

BANGLADESH UNIVERSITY OF ENGINEERING AND  
TECHNOLOGY

---

**Polycrystallinity and Grain Size Effects  
on Tensile and Creep Behaviour of  
Tungsten Nanomaterial**

---

*Author:*

Sourav Saha

Student no.: 1015102051

*Supervisor:*

Dr. Mohammad Abdul Motalab

*A thesis submitted to the Department of Mechanical Engineering, BUET  
in partial fulfillment of the requirements for the degree of Master of Science*

*in*

Mechanical Engineering

November 2017



## Declaration of Authorship

I, Sourav Saha, declare that this thesis titled, “Polycrystallinity and Grain Size Effects on Tensile and Creep Behaviour of Tungsten Nanomaterial” and the work presented in it are my own. I confirm that:

- This work is done wholly or mainly while in candidature for a part of undergraduate degree at this University.
- Where any part of this thesis has previously been submitted for a degree or any other qualification at this University or any other institution, this has been clearly stated.
- Where I have consulted the published work of others, this is always clearly attributed.
- Where I have quoted from the work of others, the source is always given. With the exception of such quotations, this thesis is entirely my own work.
- I have acknowledged all main sources of help.
- The thesis is based on the research works done by myself along with others and I have acknowledged the support of others.

Signed:

---

Date:

---

## Certificate of Approval

This thesis titled "Polycrystallinity and Grain Size Effects on Tensile and Creep Behaviour of Tungsten Nanomaterial" submitted by Sourav Saha, Roll No: 1015102051 P, Session **October, 2015** has been accepted as satisfactory in partial fulfillment of the requirement for the degree of MASTER OF SCIENCE IN MECHANICAL ENGINEERING on **November 14, 2017**.

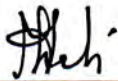
### BOARD OF EXAMINERS



27.11.17

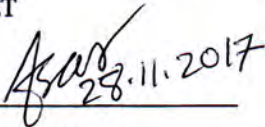
Dr. Mohammad Abdul Motalab  
Associate Professor  
Department of Mechanical Engineering  
BUET

Chairman (Supervisor)



Dr. Mohammad Ali  
Professor and Head  
Department of Mechanical Engineering  
BUET

Member(Ex-officio)



28.11.2017

Dr. Md. Afsar Ali  
Professor  
Department of Mechanical Engineering  
BUET

Member



Dr. A.K.M. Masud  
Professor  
Department of Industrial and Production Engineering  
BUET

External

*“Know that all beautiful, glorious, and mighty creations spring from but a spark of My splendor.”*

Bhagavad Gita (10.41)

# *Abstract*

Though use of Tungsten ( $W$ ) as nanomaterial has been increasing there is lack of knowledge on its failure behaviour and other mechanical properties at nanoscale. In order to investigate plasticity and creep mechanism at the nanoscale, single and polycrystalline nanowires and nanocubes of  $W$  are studied in this work. In case of single and polycrystalline nanowire, diameter, temperature, loading orientation, and grain size are varied to see the resulting impact on the deformation mechanism using EAM potential and a constant strain rate of  $10^9 \text{ s}^{-1}$ . Results of the analyses indicate domination of twinning deformation over dislocation in single crystal nanowires. However, in polycrystalline nanowires, the failure mechanism is governed by the twin-grain boundary interaction. Additionally, strength of polycrystalline nanowires follow inverse Hall-Petch rule. In the latter part of the thesis, nature of creep in nanocrystalline tungsten and factors that govern creep mechanism such as grain size, temperature, and applied stress are studied through atomistic simulations. From the simulations, it has been observed that the creep mechanism in nanocrystalline tungsten is contingent on the applied stress as the creep mechanism varies from lattice diffusion to grain boundary diffusion creep eventually to dislocation-creep with higher stress. Moreover, temperature and grain refinement seem to aid the creep phenomenon at the nanoscale. It is also identified that for very large values of stress and temperature, the power-law fails to define the creep in nc-tungsten. To quantify the propensity and mechanism of creep in nanocrystalline tungsten, stress and grain size exponents are determined in addition to the time evolution of strain and mean square displacement. Finally, atomistic features of deformation are analyzed which evince the simulation results.

# *Acknowledgements*

First of all, I would like to thank my honorable supervisor, **Dr. Mohammad Abdul Motalab** for his continuous support and guidance for this work. Without him the thesis would remain as some fragments of my imagination. I would like to thank the **Department of Mechanical Engineering, Bangladesh University of Engineering and Technology, Dhaka** for providing me the computational resources required for this work. I am grateful to **Dr. Monon Mahboob** for his valuable suggestions on my work. Finally, I am thankful to my family members for their encouragement and love.

# Contents

<b>Declaration of Authorship</b>	<b>i</b>
<b>Certificate of Approval</b>	<b>ii</b>
<b>Abstract</b>	<b>iv</b>
<b>Acknowledgements</b>	<b>v</b>
<b>Contents</b>	<b>vi</b>
<b>List of Figures</b>	<b>vii</b>
<b>List of Tables</b>	<b>viii</b>
<b>Abbreviations</b>	<b>ix</b>
<b>Physical Constants</b>	<b>x</b>
<b>Symbols</b>	<b>xi</b>
<b>1 Introduction</b>	<b>1</b>
1.1 Nanomaterials . . . . .	1
1.2 Crystal Systems . . . . .	4
1.3 Miller Indices . . . . .	6
1.4 Polycrystalline Materials . . . . .	6
1.5 Nature of Deformation in BCC Crystals . . . . .	7
1.6 Deformation in Polycrystalline Materials . . . . .	10
1.7 Creep Deformation . . . . .	12
1.8 Literature Review . . . . .	13
1.8.1 Single Crystal Nanowire . . . . .	14

1.8.2	Polycrystalline Nanowire . . . . .	15
1.8.3	Creep in Nanomaterials . . . . .	15
1.9	Objectives of the Work . . . . .	16
1.10	Outline of the Thesis . . . . .	17
<b>2</b>	<b>Simulation Methodology</b>	<b>19</b>
2.1	Molecular Dynamics . . . . .	19
2.1.1	Advantages of MD . . . . .	20
2.1.2	Disadvantages of MD . . . . .	21
2.2	Steps of MD Simulation . . . . .	21
2.2.1	Initialization . . . . .	22
2.2.2	Force field . . . . .	23
2.2.3	EAM Potential . . . . .	24
2.2.4	Force Calculation . . . . .	25
2.2.5	Energy Minimization . . . . .	26
2.2.6	Boundary Conditions . . . . .	26
2.3	Statistical Ensembles . . . . .	27
2.4	Physical Modeling . . . . .	28
2.4.1	Tungsten Nanowire . . . . .	28
2.4.1.1	Single Crystal . . . . .	28
2.4.1.2	Polycrystalline . . . . .	29
2.5	Creep Analysis Model . . . . .	29
2.6	Calculation of Physical Properties . . . . .	30
2.6.1	Stress . . . . .	30
2.6.2	Mean Square Displacement (MSD) . . . . .	31
2.6.3	Pressure and Temperature . . . . .	31
2.6.4	Strain . . . . .	31
2.7	Validation of Potential . . . . .	32
2.8	Simulation and Visualization . . . . .	33
2.9	Summary . . . . .	33
<b>3</b>	<b>Tensile Behavior of <math>W</math></b>	<b>34</b>
3.1	Introduction . . . . .	34
3.2	Single Crystal Nanowire . . . . .	34
3.2.1	Effect of Temperature . . . . .	35
3.2.2	Effect of Diameter . . . . .	36
3.2.3	Effect of Crystal Orientation . . . . .	39
3.2.4	Failure Mechanism . . . . .	41
3.3	Polycrystalline Nanowire . . . . .	43
3.3.1	Impact of Grain Size . . . . .	43
3.3.2	Impact of Diameter . . . . .	46
3.3.3	Impact of Temperature . . . . .	47



---

3.3.4	Failure Mechanism . . . . .	47
3.4	Summary . . . . .	52
<b>4</b>	<b>Creep Behavior of <math>W</math> at Nanoscale</b>	<b>53</b>
4.1	Introduction . . . . .	53
4.1.1	Nature of Creep Curves . . . . .	53
4.1.2	Impact of Grain Size . . . . .	57
4.1.3	Impact of Stress . . . . .	59
4.1.4	Impact of Temperature . . . . .	61
4.1.5	Creep Mechanism . . . . .	62
4.2	Summary . . . . .	67
<b>5</b>	<b>Conclusions</b>	<b>68</b>
5.1	Tensile Behavior of Single Crystal Nanowire . . . . .	68
5.2	Tensile Behavior of Polycrystalline Nanowire . . . . .	69
5.3	Creep in Nanocrystalline Tungsten . . . . .	69
	 <b>Bibliography</b>	 <b>71</b>

# List of Figures

1.1	TEM bright field image of Tungsten nanoparticles which are zero dimensional nanomaterials. . . . .	3
1.2	TEM images of A) Nanowires (1D nanostructures), B) 2D branched nanostructures, C) Nanocones (3D nanostructures). . . . .	4
1.3	A sample unit cell with the basis vectors and angles. . . . .	5
1.4	Body-centered cubic unit cell. . . . .	5
1.5	An example cubic cell to explain Miller indices. . . . .	7
1.6	Resolved shear stress for uniaxially applied stress. . . . .	8
1.7	Stacking sequence in bcc metals viewed for {112} planes. (a) Orthographic projection, (b) Projection of (112) planes on a (110) plane. . . . .	9
1.8	Twinning deformation in materials. Above and below the x-y plane atoms are deformed like mirror image of each other. . . . .	10
1.9	Sequential motion of $\frac{1}{6} \langle 111 \rangle$ twin on {112} planes to create twin boundary in bcc material. . . . .	11
1.10	Different stages of creep deformation. . . . .	13
2.1	Assumption of molecular dynamics. . . . .	20
2.2	Steps to solve molecular dynamics simulation. . . . .	22
2.3	Comparison between pair potential and multi-body potential. . . . .	23
2.4	The figure shows how periodic boundary condition works. . . . .	24
2.5	Schematic diagram of the single crystal Tungsten nanowire with length $L$ and diameter $D$ . . . . .	28
2.6	Schematic diagram of the (a) sample nanowire and (b) diameter and length of sample nanowire. . . . .	29
2.7	Schematic diagram of the cubic sample of tungsten nano-crystal with dimensions. . . . .	30
2.8	Variation of potential energy per atom with temperature using EAM potential of this work. . . . .	32
3.1	Stress vs strain diagram for single crystal Tungsten nanowires of 2 nm diameter at different temperatures. . . . .	35
3.2	Variation of Young's modulus with temperature for single crystal Tungsten nanowire of 2 nm diameter. . . . .	36

3.3	Variation of yield stress with temperature for single crystal Tungsten nanowire of 2 nm diameter. . . . .	37
3.4	Stress vs strain diagram for single crystal Tungsten nanowires of different diameters at 300 K temperature. . . . .	37
3.5	Variation of Young's modulus with diameters for single crystal Tungsten nanowire at 300 K temperature. . . . .	38
3.6	Variation of yield stress with diameters for single crystal Tungsten nanowire at 300 K temperature. . . . .	39
3.7	Results for loading along different crystal orientations at 300 K temperatures and 2 nm diameter. . . . .	40
3.8	Atomistic configurations of nanowire of 3 nm diameter at 300 K at different stages of uniaxial tensile test. . . . .	41
3.9	Atomistic configurations of nanowire of 4 nm diameter at 300 K at different stages of uniaxial tensile test. . . . .	42
3.10	Atomistic configurations of nanowire of 2 nm diameter at 300 K for loading at $\langle 111 \rangle$ direction during uniaxial tensile test. . . . .	43
3.11	(a) Stress vs strain plot, and (b) Variation of Young's modulus for different grain sizes at 10 K temperature and for 5 nm diameter nanowire. . . . .	45
3.12	(a) Variation of yield stress, and (b) modulus of resilience for different grain sizes at 10 K temperature and for 5 nm diameter nanowire. . . . .	45
3.13	(a) Stress vs strain plot, and (b) Variation of Young's modulus with diameter of nanowires at 10 K and 6.79 nm average grain size. . . . .	46
3.14	(a) Variation of yield stress, and (b) modulus of resilience with diameter of nanowires at 10 K and 6.79 nm average grain size. . . . .	47
3.15	(a) Stress vs strain plot, and (b) Variation of Young's modulus with temperatures for nanowire of 5 nm diameter and 6.79 nm grain size. . . . .	48
3.16	(a) Variation of yield stress, and (b) modulus of resilience with temperature for nanowire of 5 nm diameter and 6.79 nm average grain size. . . . .	48
3.17	Atomistic configurations of nanowire of 2 nm diameter and 6.79 nm average grain size at 10 K at different stages of uniaxial tensile test. . . . .	49
3.18	Atomistic configurations of nanowire of 5 nm diameter and 14.91 nm average grain size at 10 K at different stages of uniaxial tensile test. . . . .	49
3.19	Atomistic configurations of nanowire of 5 nm diameter and 6.79 nm average grain size at 10 K at different stages of uniaxial tensile test. . . . .	50
3.20	Atomistic configurations of nanowire of 5 nm diameter and 4.63 nm average grain size at 10 K at different stages of uniaxial tensile test. . . . .	51
4.1	Creep curves for different applied stresses at a) 1600 K, b) 1800 K, c) 2000 K, and d) 2200 K for grain size of 4.76 nm. . . . .	54
4.2	Creep curves for different applied stresses at a) 1600 K, b) 1800 K, c) 2000 K, and d) 2200 K for grain size of 3.57 nm. . . . .	55
4.3	Creep curves for different applied stresses at a) 1600 K, b) 1800 K, c) 2000 K, and d) 2200 K for grain size of 2.86 nm. . . . .	56

---

4.4	Creep curves for different applied stresses at a) 1600 K, b) 1800 K, c) 2000 K, and d) 2200 K for grain size of 2.38 nm. . . . .	57
4.5	Comparison of creep curves between single-crystal and nanocrystalline tungsten at 1800 K under 5 GPa stress. . . . .	58
4.6	Creep curve calculated for Copper by Wang et al. . . . .	58
4.7	Variation of steady-state creep rate with inverse grain size for applied stress at a) 1600 K, b) 1800 K, c) 2000 K, and d) 2200 K. . . . .	59
4.8	Variation of steady-state creep rate with applied stress for different grain sizes at a) 1600 K, b) 1800 K, c) 2000 K, and d) 2200 K . . . . .	61
4.9	Variation of steady-state creep rate with applied stress at grain sizes of a) 4.76 nm, b) 3.57 nm , c) 2.86 nm, and d) 2.38 nm . . . . .	62
4.10	Mean square displacements of the $W$ atoms for a) 4.76 nm, b) 3.57 nm , c) 2.86 nm, and d) 2.38 nm average grain size under 3.5 GPa stress. . . . .	63
4.11	Diffusion coefficient as a function of temperature and grain size under 3.5 GPa applied stress. . . . .	64
4.12	Change in stress exponent for gradually increasing stresses for grain size of 4.76 nm at 1800 K. . . . .	64
4.13	Atomistic configurations of $W$ with grain size of 3.57 nm at 1800 K under 3 GPa stress. a) at $t = 0$ ps, b) at $t = 100$ ps, and c) at $t = 200$ ps. . . . .	65
4.14	Atomistic configurations of $W$ with grain size of 2.86 nm at 2200 K under 4 GPa stress. a) at $t = 0$ ps, b) at $t = 100$ ps, and c) at $t = 200$ ps. . . . .	65

# List of Tables

1.1	Seven crystal systems. . . . .	6
3.1	Young's modulus and yield stress of nanowires with 2 nm diameter at different crystal orientations. . . . .	40
4.1	Grain size exponents ( $p$ ) for different temperatures and stresses. . . . .	60
4.2	Stress exponents ( $n$ ) for different temperatures and grain sizes. . . . .	60

# Abbreviations

<b>CNT</b>	<b>Carbon Nano Tube</b>
<b>DFT</b>	<b>Density Functional Theory</b>
<b>EAM</b>	<b>Embedded Atom Method</b>
<b>FEM</b>	<b>Finite Element Method</b>
<b>SSCR</b>	<b>Steady State Creep Rate</b>
<b>TEM</b>	<b>Transmission Electron Microscopy</b>

# Physical Constants

Gravitational acceleration,  $g = 9.81 \text{ ms}^{-2}$

Boltzmann constant,  $k_B = 1.38 \times 10^{-23} \text{ JK}^{-1}$

# Symbols

$a$	Lattice constant	$A^0$
$b$	Basis vector	
$d$	Grain size	$nm$
$l$	Length of nanowire	$nm$
$r$	Distance between atoms	$A^0$
$t$	Time	$s$
$v$	Velocity of particles	$ms^{-1}$
$D$	Diameter of nanowire	$nm$
$K$	Kinetic energy	$J$
$N$	Number of particles	
$P$	Pressure	$Pa$
$T$	Temperature	$K$
$\epsilon$	Strain	
$\tau$	Resolved shear stress	$MPa$
$\sigma$	Normal stress	$MPa$



*Dedicated to my mother...*

# Chapter 1

## Introduction

Proliferation of nanotechnology is perhaps one of the most striking advancements of past decades. Use of nanotechnology encompasses fields of biology, medicine, physics, materials science, and engineering. Prescience of famous physicist Richard Feynman, “There is plenty of room at the bottom” [2], has become true in the advent of the twenty-first century. Because of the interdisciplinary nature of nanotechnology physicists, chemists, engineers frequently collaborate for new inventions. Mechanical engineers are particularly interested in the study of mechanics and failure mechanism at the nanoscale. Such studies are of vital importance as from the study of nanomechanics and failure at nanoscale one can predict the possibility and mode of deformation at larger scale [3].

### 1.1 Nanomaterials

There is no ubiquitous definition of nanomaterials that points to a specific class of materials. Rather nanomaterials are defined on the basis of dimension [4]. Nanomaterials are defined as the materials that possess dimension in the order of billionth of a meter [5]. Usually, a nanomaterial is characterized as a material with dimension in the order of 1 to 100 nm. So the definition and use are contrasting as practically sometimes some micrometer-sized devices are also identified as nanomaterials [5]. The word *nano*

comes from the Latin word *nanus* meaning dwarf [6]. Though dwarfed by size, nanomaterials are not be looked down in terms of its properties. At nanoscale, materials show elevation in strength, ductility, corrosion resistance, and wear resistance due to lack of defects. Multiscale modeling techniques have enabled scientists to predict material properties in bulk materials gaining insight from their nanoscale counterpart.

Advantages of nanomaterials have prompted it's different uses. For example [7]:

- \* New generation computer chips.
- \* Improved insulation materials.
- \* Low-cost, flat-panel displays.
- \* High energy density batteries.
- \* Aerospace components.
- \* Ductile, machinable cermaics.
- \* Longer-lasting medical implants. etc.

Nanomaterials are classified into four major categories [8]:

1. **Zero-dimensional Nanomaterials:** Zero-dimensional materials are those nanomaterials that have no geometric dimension (like particles). Example of such nanomaterials are nanoparticles, quantum dots, etc. These materials can be amorphous or crystalline. They exhibit various shapes and forms. These types of materials are used extensively in light emitting diodes (LED), solar cells, and lasers [8]. Figure 1.1 [9] shows an example of zero dimensional materials.
2. **One-dimensional Nanomaterials:** One-dimensional nanomaterials are those materials whose one dimension can be out of nanoscale (greater than 100 nm) (see, Figure 1.2 A) [8]). Examples of one dimensional nanomaterials are nanotubes, nanowires, and nanorods. One dimensional materials can also be amorphous or crystalline and single or polycrystalline. These materials play an important role in fabrication of electronic and opto-electronic devices.

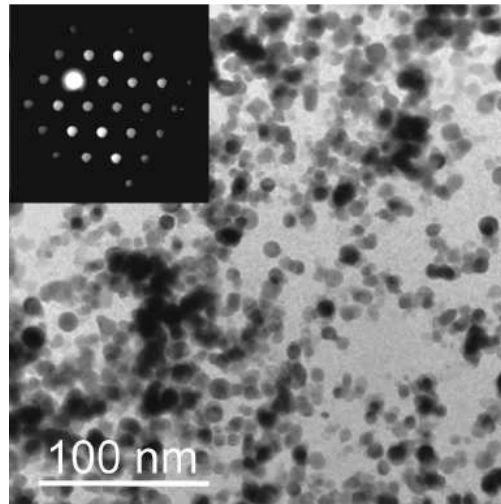


FIGURE 1.1: TEM bright field image of Tungsten nanoparticles which are zero dimensional nanomaterials.

3. **Two-dimensional Nanomaterials:** Two-dimensional nanomaterials are those which allow two of their dimensions to be out of nanoscale. Nanofilms, nanolayers, nanodiscs, and nanocoatings are examples of two dimensional nanomaterials (refer to Figure 1.2 B)). Two dimensional nanomaterials can be deposited as substrate. These are used as single or multilayer structures. Two dimensional nanomaterials have become focal point of many research due to their unique properties. These materials have novel applications in sensors and nanodevices.
4. **Three-dimensional Nanomaterials:** Dimensions of three-dimensional or bulk nanomaterials are not confined to nanoscale. This means either or all of the three dimensions can exceed the limit of 100 nm. These are called nanomaterials only because they possess physical properties of a nanocrystalline structure. It can be single crystal or polycrystalline. Nanocrystalline structures are identified as three-dimensional nanomaterials comprising of single crystals oriented in different directions. Behaviour of such nanomaterials depend on their size and surface morphology. Hence, research on the fabrication of such materials is of paramount importance. Higher specific surface area compared to volume enables these materials to provide absorption sites for other atoms in nanoscale applications. Moreover, deformation behaviour at nanoscale can be used to predict properties of the bulk counterparts. Figure 1.2 C) shows an example of Three-dimensional nanomaterials.

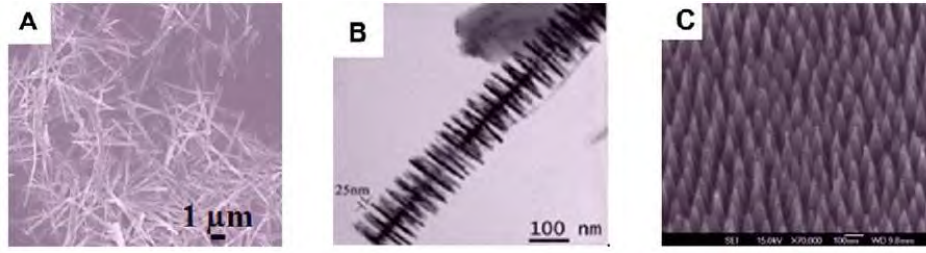


FIGURE 1.2: TEM images of A) Nanowires (1D nanostructures), B) 2D branched nanostructures, C) Nanocones (3D nanostructures).

## 1.2 Crystal Systems

In order to understand the mechanism of failure in the crystalline structure, one needs to identify the crystal structure of the material. Solids can be both crystalline and amorphous. In crystalline materials, atoms are arranged in regular pattern. On the other hand, in amorphous materials atoms are arranged randomly. Arrangement of atoms in a crystalline solid can be explained with the concepts of unit cell and Bravais lattice. Unit cells are the most fundamental building blocks of a crystal structure [10]. The entire crystal system can be built by repeating this block in three non-coplanar directions through translation. The shape and arrangement of the unit cells describe a crystal system completely. Different arrangements of unit cells in crystalline structures can be attained by space lattices known as Bravais lattice [10, 11]. Points in the Bravais space lattice are so arranged that any point  $r(n_1, n_2, n_3)$  can be traced from any other point  $r(0, 0, 0)$  in space by the translational operation [10],

$$r(n_1, n_2, n_3) = r(0, 0, 0) + \vec{R} \quad (1.1)$$

Here,  $\vec{R} = n_1\vec{b}_1 + n_2\vec{b}_2 + n_3\vec{b}_3$  is the translational basis vector and  $n_1, n_2$ , and  $n_3$  are arbitrary integers. The parallelepiped enclosed by  $\vec{b}_1, \vec{b}_2$ , and  $\vec{b}_3$  is called the unit cell [10].

Figure 1.3 shows the three basis vectors building a parallelepiped with three angles  $\alpha, \beta$ , and  $\gamma$  [10]. Different combinations of these basis vectors and angles give rise to seven lattice systems with fourteen Bravais lattice. The seven lattice systems are shown in Table 1.1. In this work, body-centered cubic Tungsten is discussed. In the cubic lattice systems the the basis vectors  $b_1, b_2$ , and  $b_3$  have same magnitude and the angles

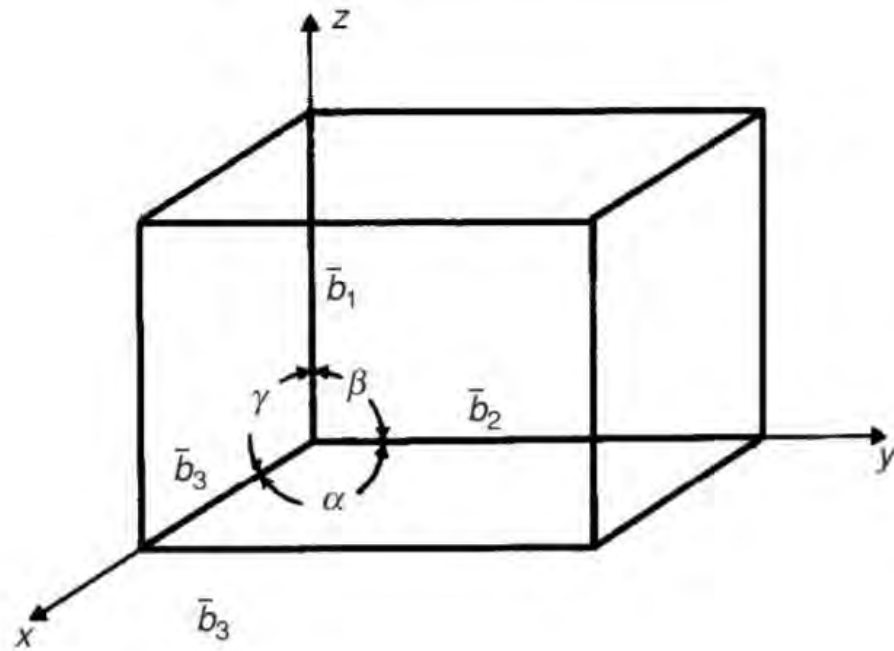


FIGURE 1.3: A sample unit cell with the basis vectors and angles.

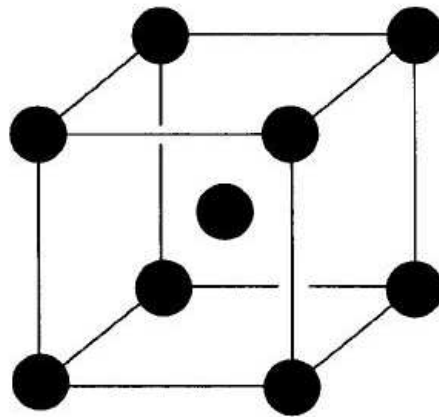


FIGURE 1.4: Body-centered cubic unit cell.

$\alpha = \beta = \gamma = 90^\circ$ . Body-centered cubic structures are cubic structures with atoms at each vertex and an additional atom at the center of the unit cell as shown in Figure 1.4[11].

Body-centered cubic structure of materials cause unique deformation behaviour at the nanoscale [11]. Present work tries to find such behaviour in the failure mechanism of body-centered cubic Tungsten material.

Crystal system	Lattice parameters	Inter-facial angles
Cubic	$b_1 = b_2 = b_3$	$\alpha = \beta = \gamma = 90^0$
Tetragonal	$b_1 = b_2 \neq b_3$	$\alpha = \beta = \gamma = 90^0$
Orthorhombic	$b_1 \neq b_2 \neq b_3$	$\alpha = \beta = \gamma = 90^0$
Monoclinic	$b_1 \neq b_2 \neq b_3$	$\alpha = \beta = 90^0 \neq \gamma$
Triclinic	$b_1 \neq b_2 \neq b_3$	$\alpha \neq \beta \neq \gamma \neq 90^0$
Hexagonal	$b_1 = b_2 \neq b_3$	$\alpha = \beta = 90^0, \gamma = 120^0$
Rhombohedral	$b_1 = b_2 = b_3$	$\alpha = \beta = \gamma \neq 90^0$

TABLE 1.1: Seven crystal systems.

### 1.3 Miller Indices

In order to specify the crystal orientation and crystal planes Miller indices are generally used. In order to understand the concept of Miller indices, one may refer to the Fig. 1.5 [11]. In the figure a reference cubic unit cell of dimension  $a$  is taken (OABC). With respect to this unit cell one can find the Miller indices of the other planes and directions in any material. Let us consider a plane  $A'B'C'$  and the dimensions  $OA' = 2a$ ,  $OB' = 3a$ , and  $OC' = 3a$ . Now the reciprocals of the intercepts of the plane can be written as  $(\frac{OA}{OA'}, \frac{OB}{OB'}, \frac{OC}{OC'})$  or  $(\frac{a}{2a}, \frac{a}{3a}, \frac{a}{3a})$ . By definition the Miller indices are these reciprocals of the intercepts. However, by definition Miller indices can not be fraction. So multiplying all the ratios by 6 we get the final Miller indices of the plane  $A'B'C'$  as (322). If the intercept of any plane is negative a bar (for example,  $(1\bar{1}\bar{1})$ ) sign is used. On the contrary, the direction of any crystal plane is simpler to denote. In such one needs to take smallest multiple of the unit cell's dimension in any one of the three mutually perpendicular axes. For example, if one considers the Miller indices of direction  $OA'$ , it will be  $(\frac{2a}{a}, \frac{0}{a}, \frac{0}{a})$  or [200]. However, as one needs to take the smallest integer as the index, the original Miller indices of  $OA'$  becomes [100]. A group of crystallographic directions are collectively expressed by  $\langle \rangle$  sign while group of planes by  $\{ \}$  sign.

### 1.4 Polycrystalline Materials

The main difference between single and polycrystalline materials is that in the polycrystalline materials atoms are arranged in grains of different orientations. Each grain

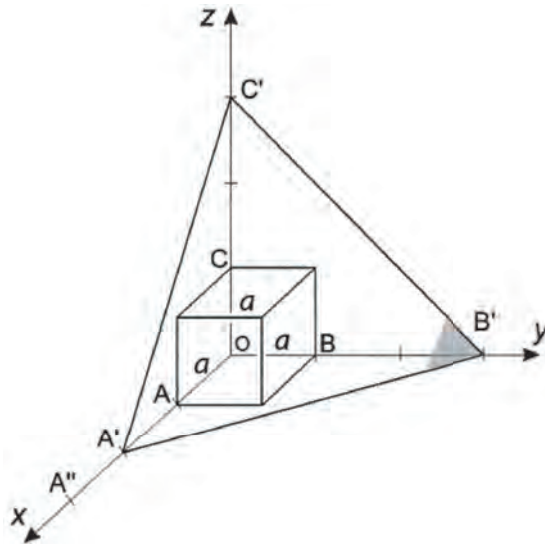


FIGURE 1.5: An example cubic cell to explain Miller indices.

contains consistent crystal structure. However, the orientation of the grain varies making the polycrystalline material an aggregate of several crystals [11, 12]. Failure mechanism in single and polycrystalline forms of the same material differs significantly due to the difference in the critical resolved shear stress (CRSS) during failure. Most of the naturally occurring materials contain grains and grain boundaries which act as a planar defect in the materials. These defects influence the deformation mechanism of the nanomaterial significantly by interacting with the dislocation and acting as sources and sinks of void and other defects. One of the major objectives of this work is to identify how grain boundaries in the nanocrystalline Tungsten impact the failure mechanism in the material.

## 1.5 Nature of Deformation in BCC Crystals

In order to understand the mechanism of deformation in Tungsten and how it differs from conventional materials, one needs to understand the basic mechanism of deformation in bcc crystals at first. Plastic deformation in solids occurs either through dislocation or twinning. However, the preference of dislocation or twinning depends on various conditions including loading orientation, temperature, strain rate, etc. The most fundamental concept here is the idea of critical resolved shear stress (CRSS). It can be defined as the critical value of resolved shear stress for which a crystalline material will



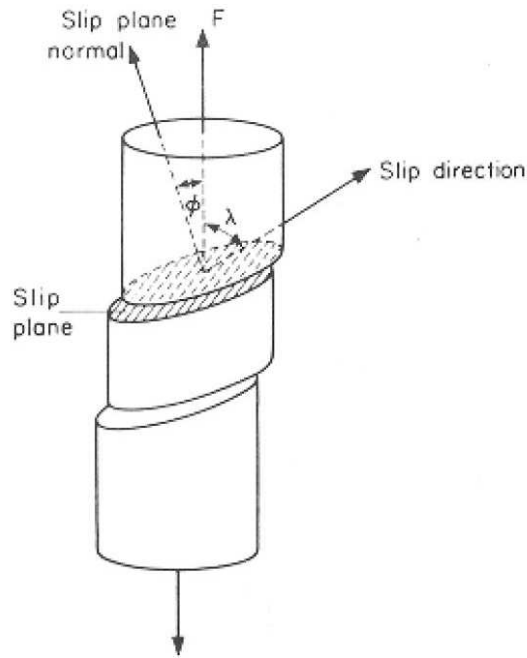


FIGURE 1.6: Resolved shear stress for uniaxially applied stress.

deform. Figure 1.6 clarifies its definition [11]. In the figure, a force  $F$  is applied uniaxially to a cylindrical sample. The plane on which stress  $\sigma$  is to be measured has an area  $A$ . If the force makes an angle  $\lambda$  with the plane and  $\phi$  with the normal of the area, resolved shear stress on the area is given by

$$\tau = \sigma \cos \phi \cos \lambda \quad (1.2)$$

When the resolved shear stress reaches a critical value  $\tau_{cr}$  slip or twinning occurs in the material. The preferred mode of deformation depends on the Schmidt factor defined as  $\cos \phi \cos \lambda$ . If it requires less stress for twinning, deformation by twinning will occur while if the stress required for dislocation is smaller, dislocation will prevail. Dislocation in bcc crystal structure can be straight or edge, screw or mixed in nature. One of the most striking features in bcc metals is that the slip plane is not well defined for these materials. Normally, the slip occurs along the closed packed direction [11].

In body-centered cubic (bcc) materials, the atoms are located at the corners of the unit cell and one at the middle position of  $(\frac{1}{2}, \frac{1}{2}, \frac{1}{2})$ , as shown in Figure 1.4 [11]. The atoms of such unit cell touch along the  $\langle 111 \rangle$  line. This is why in bcc crystal structure the closed-packed direction is  $\langle 111 \rangle$ . One can observe the stacking sequence and get

an idea on the packed planes from Figure 1.7. Figure 1.7 (a) shows the orthographic projection and for convenience a planar projection of  $(11\bar{2})$  plane is shown in Figure 1.7 (b). As can be seen from the figures in  $[111]$  directions there is the highest number of atoms. Moreover the stacking sequence changes for 100 planes from ABABAB... to the 112 planes in ABCDEFA.... This change in sequence of stacking of atoms in the plane plays vital role in the deformation of bcc crystals. However, there can be multiple planes containing same closed-packed  $\langle 111 \rangle$  crystal direction and the difference in applied stress to activate slip is small. Shortest lattice vector for deformation or Burgers vector for dislocation in bcc metals is  $\frac{1}{2} \langle 111 \rangle$ . Three  $\{110\}$  planes, three  $\{112\}$ , and six  $\{123\}$  planes intersect along the same  $\langle 111 \rangle$  direction. So we see that there is an uncertainty about the path of deformation propagation as all the plane contains closed-pack direction. Hence, depending on the applied stress, a screw dislocation can move in different planes. This creates a number of possibilities for the motion of dislocation in bcc metals. Moreover, there is asymmetry in the motion of dislocation on the same crystallographic plane.

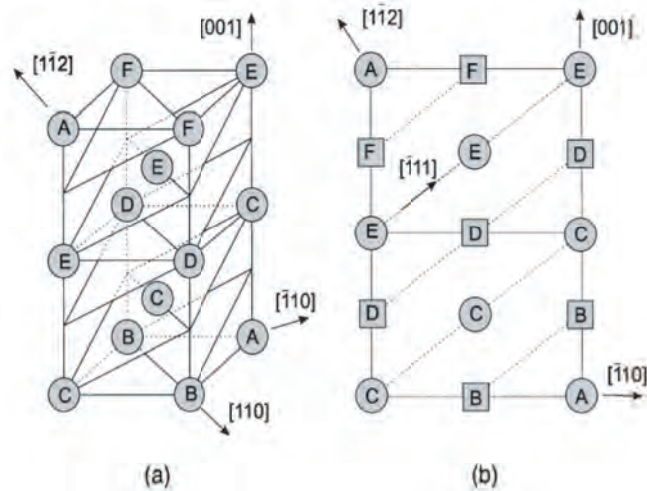


FIGURE 1.7: Stacking sequence in bcc metals viewed for  $\{112\}$  planes. (a) Orthographic projection, (b) Projection of  $(11\bar{2})$  planes on a  $(110)$  plane.

The other mode of deformation in the bcc metals is the deformation by twinning. In case of twinning, atoms deform in such a way that the deformed and undeformed parts are mirror images of each other (see Figure 1.8 [11]). In bcc metals, twinning occurs under low temperature or high strain rates. The source of twinning deformation is the displacement of  $\frac{1}{6} \langle 111 \rangle$  on every successive  $\{112\}$  planes [11]. The mechanism can be illustrated taking help from the Figure 1.7 (a) and (b). Now if one looks at the Figure

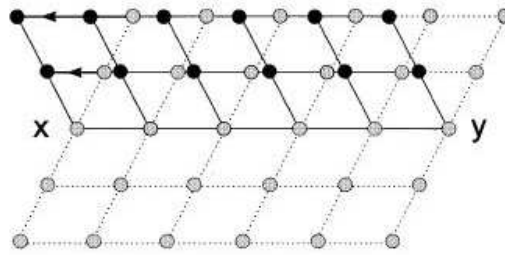


FIGURE 1.8: Twinning deformation in materials. Above and below the x-y plane atoms are deformed like mirror image of each other.

Figure 1.7 (b), one can see that on the  $\{11\bar{2}\}$  planes, along the  $\langle 111 \rangle$  direction the atoms are similar in stacking (either all are F or all are D or all are C, etc.). Hence in order to produce a twin boundary all one need is to push by applying shear any one of the layers slight out of place along the  $\langle 111 \rangle$  direction. This will create a stacking fault or the boundary and on the both sides of this boundary, the atoms' stacking will be similar! Each motion of  $\frac{1}{6} \langle 111 \rangle$  creates a stacking fault which ultimately creates a twin boundary.

Li et al. [13] captured an excellent sequential image of this phenomenon. In Figure 1.9 it is presented. In this figure, red lines indicated the thickness of the twin boundary and yellow lines indicate atoms in motion. One can see that at 19041.1 ps, the first  $\langle 111 \rangle$  motion occurs on the  $\{112\}$  plane. Subsequently, a twin boundary emerges. Now the step height between two neighbour  $\{112\}$  plane is  $\frac{a}{\sqrt{6}}$  where  $a$  is the unit cell dimension. Thus the resulting Burgers vectors will be  $\frac{1}{6} \langle 111 \rangle$ . In subsequent steps of the Figure 1.9 one can see that sequential motion of  $\frac{1}{6} \langle 111 \rangle$  or movement of atoms along the  $\langle 111 \rangle$  direction on the  $\{112\}$  plane creating or growing the twin boundary in the bcc material.

## 1.6 Deformation in Polycrystalline Materials

Nature of deformation in polycrystalline materials is fundamentally different from the single crystal materials. Because of the randomly distributed grains, in polycrystalline materials the CRSS does not play a significant role in deformation like the single crystals. Moreover, the grain boundaries act as a barrier to the motion of dislocations creating a surge in the stress developed inside the material. This stress is relaxed by local

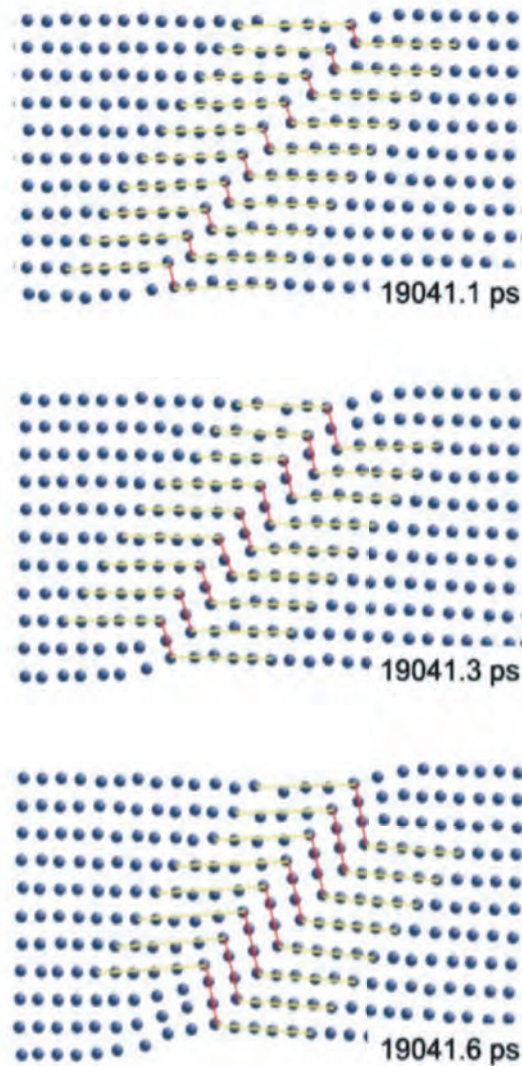


FIGURE 1.9: Sequential motion of  $\frac{1}{6} \langle 111 \rangle$  twin on  $\{112\}$  planes to create twin boundary in bcc material.

plastic deformation. The grain boundaries also act as the sources of voids and cracks which help initiate the failure. Temperature and grain size play a vital role in the deformation of the polycrystalline materials. Especially the impact of grain size has been under scrutiny by many researchers. It has been found that as the grain size is reduced in the polycrystalline materials, the strength of such materials increases. It is proposed by the experimental works of Hall and Petch [14, 15] that the grain size and yield strength of polycrystalline material are related by the following relationship,

$$\sigma_y = \sigma_0 + \frac{k}{d^{0.5}}. \quad (1.3)$$

Here  $\sigma_y$  is the yield stress,  $\sigma_0$  is the friction stress in the absence of grain boundaries,  $d$  is the grain size and  $k$  is a constant. This supports the old phrase “Smaller is stronger.” However, the statement prove to be true only up to certain critical grain size. Below this critical grain size, further grain refinement actually softens the material [16–20]. Moreover, the mechanism of plastic deformation turns from dislocation dominated to grain boundary sliding or grain rotation as the grain size becomes smaller [18]. This phenomenon is christened as reverse or inverse Hall-Petch relationship by many authors [21].

## 1.7 Creep Deformation

Under high temperature and static mechanical stress creep is a common mode of deformation in materials. It is time dependent and permanent deformation of material [22]. Creep is an undesirable deformation of material. Creep becomes an important mode of deformation when the temperature is above 0.4 of the absolute melting temperature. Moreover, at nanoscale creep can be influenced by the grain size. Creep behaviour of any material can be observed on the creep curve. A creep curve is constructed by plotting the creep strain against the time for a constant applied mechanical stress under a certain temperature. A typical creep curve is shown in Figure 1.10. There are three distinct stages of the creep curve. Primary or transient creep is the first stage which occurs right after the instantaneous deformation by applied load. This stage shows a gradual weakening of the creep rate suggesting strain hardening. Next comes the steady-state creep or secondary creep. At this stage the creep rate remains more or less constant. This is the more lasting stage of creep deformation. At this stage there is a competition between strain hardening and recovery. Finally, tertiary creep stage occurs when the creep rate is accelerated to ultimate failure or rupture.

Previous studies on nanoscale creep behaviour of materials suggest that there is a relationship between applied stress, grain size, and temperature to which the materials are

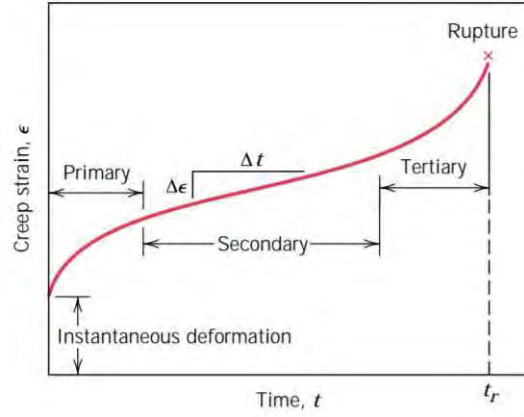


FIGURE 1.10: Different stages of creep deformation.

exposed to. Relation of these three parameters with steady-state creep rate is expressed by Bird-Dorn-Mukherjee equation [23] as,

$$\dot{\epsilon} = \frac{AD_0Gb}{k_B T} \left(\frac{b}{d}\right)^p \left(\frac{\sigma}{G}\right)^n \exp\left(-\frac{\delta Q}{k_B T}\right) \quad (1.4)$$

where  $\dot{\epsilon}$  is the steady-state creep rate (SSCR),  $A$  is a dimensionless constant,  $D_0$  is the diffusion coefficient,  $G$  is the shear modulus,  $b$  is the Burgers vector,  $k_B$  is the Boltzmann's constant,  $T$  is the absolute temperature,  $d$  is the grain size,  $\sigma$  is the applied stress,  $\delta Q$  is the activation energy for thermal-activated process,  $p$  and  $n$  are the grain size and stress exponents, respectively.

## 1.8 Literature Review

In order to understand the nanoscale mechanical behaviour of Tungsten, in this work single and polycrystal nanowires are taken as samples. By analyzing the response of such nanowires under uniaxial tensile or compressive tests one can get idea regarding the processes involved in the failure of Tungsten at nanoscale. Moreover, these nanowires have practical importance too.

### 1.8.1 Single Crystal Nanowire

Because of potential use in nano- (NEMS) and micro-electromechanical systems (MEMS) metallic nanowires have become the center of many scientific investigations worldwide [24, 25]. Physical properties of metallic nanowires revealed themselves to be quite different compared to the bulk counterparts [26–28]. Many computer simulations and experiments confirmed elevation of strength and dependence of elastic properties on strain rate, size and temperature of metal nanowires [29–31]. There has been extensive research on fcc metallic nanowires. Chen and Chen [32] studied plasticity in gold nanowires under high strain rate. In their study, increase in temperature lowered the value of strength of nanowire. Other studies on gold nanowires [33–35] establish the fact that strength of gold nanowires is a strong function of diameter. *Pt* nanowires' mechanical properties were reported to be dependent on the applied strain rate and temperature [36]. Studies on *Cu* nanowires [37–39] reveal that temperature and surface defects govern the strength of the nanowires directly. *Ni* nanowires show weakening at high temperatures and strain rate dependent mechanical properties are accompanied by phase transformation [40–42]. Studies on bcc nanowires mainly involved *Fe* [43] and *Mo* [44] nanowires. Interestingly, pseudo-elastic behaviour is common in bcc metal nanowires [45]. Recently, *W* nanowires attracted the attention of scientific world due to its use in pH sensitive electrodes [46], thermo-photovoltaic applications [47] and field-emission properties [48]. Insight on the mechanical properties of *W* nanowire is provided in the work of Wang et al. [49]. In this work, *in situ* experiments proved that plastic deformation in *W* nanowire requires higher stress compared to the bulk counterpart. Moreover, they have done experiments with different loading orientations to find out that both dislocation and twinning based plastic deformations may occur in *W* nanowires based on the Schmid factor in a loading system. Molecular dynamics investigation on effect of temperature on the elastic properties of *W* nanowire [50] shows gradual weakening of tungsten nanowire with higher temperature. Moreover, due to tensile loading at an elevated temperature, a phase transition occurs near twin plane. However, preparation technique can affect the mechanical properties of *W* nanowire [51].

## 1.8.2 Polycrystalline Nanowire

Grain size and grain boundary play vital roles in determining the strength of a metallic substance. Several studies have proved that through grain refining [52] and introducing grain boundaries [53] higher strength can be achieved. The primary argument behind this higher strength is interaction of dislocation and grain boundary which creates a localized stress concentration near the grain boundaries. Moreover, the mechanism of plastic deformation turns from dislocation dominated to grain boundary sliding or grain rotation as the grain size becomes smaller [18]. However, as mentioned earlier, there is dominance of inverse Hall-Petch relation in metals. This property indicates an intrinsic inverse size effect on (opposed to the common notion of “smaller is stronger”) metal substances. Hence, a synergistic study relating the external size parameter (diameter) and internal size parameter (grain size) is necessary to identify the complete picture of deformation in a nanowire. Some studies were made to identify the deformation behaviour of different polycrystalline nanowires. A study on polycrystalline *Mo* nanowire [54] concluded that the length to diameter ratio and the grain size have profound impact on the strength of the nanowires. A significantly lower value for strength was found, compared to single crystal *Cu* nanowire, in polycrystalline nanowire [55]. Both of these works showed failure originates from the grain boundaries. A study on combined effect of grain size and diameter on mechanical properties of *Al* nanowires showed that reducing the grain size to 5 nm actually weakens the nanowire [56]. Moreover, there is a competition of different deformation mechanisms for different grain sizes and diameters of the nanowire. However, there is still debate regarding the size effect on the deformation of polycrystalline nanowire revealing the importance to make a study on *W* nanowire.

## 1.8.3 Creep in Nanomaterials

Grain size and distribution also influence the creep properties of nanomaterials [57, 58]. Creep experiments are expensive and time consuming. Hence, to understand the underlying physics of creep many researchers resort to atomistic simulations nowadays [59–61]. However, atomistic simulations are limited by the requirement of large amount



of time for creep simulation. To circumvent this problem usually atomistic simulations on creep are done at a high temperature and stress conditions [62, 63].

Molecular dynamics study on pure metals corroborates the idea of Eq. 1.4. Koblinski et al. [64] identified Coble creep as the governing creep mechanism in polycrystalline silicon under relatively high tensile stress. Yin et al. [65] observed shift in creep mechanism in nanocrystalline *Ni* depending on temperature it is exposed to. Karanjgaokar and Chasiotis [66], in their experiments, observed that nature of creep in *Au* films is controlled by the temperature it is exposed to. A combined experimental and simulation study on *Cu* shows that nano-twinned *Cu* offers greater creep resistance [60] compared to twin-free nanograined *Cu* indicating a role of grain boundaries in controlling the creep. Similar outcome was also obtained by Jiao and Kulkarni [67]. Wang et al. [59] found a critical stress level after which the grain size exponent decreases for higher stress. They argued that presence of dislocation in the initial structure and their interaction with grain boundaries gave rise to such anomaly. Transition in creep mechanism was observed in nanocrystalline *Cu* depending on temperature and applied stress [68]. Nie et al [61] observed similar transition in creep mechanism in nanocrystalline *Ni* as the temperature and stress were increased. Studies on other metals and metallic alloys suggest impact of temperature, stress and grain size on creep mechanism of materials [69–72]. However, there is no significant study on creep behavior of tungsten at nanoscale using atomistic simulation to date. Experimental studies suggest applied stress controls the creep rate of pure tungsten albeit the power-law creep is not necessarily sufficient to describe creep phenomenon [73]. Robinson and Sherby [74] divided creep studies on tungsten in two categories-high temperature (above 2000 °C) and low temperature creep (below 2000 °C). The low temperature creep showed stress exponent  $n = 7$  which indicates breakdown of power-law relation. Using molecular simulation one can observe exact reasons of such anomaly. This makes the analysis more important.

## 1.9 Objectives of the Work

The present work has two distinct sections focusing on two different phenomena to gain insight into the atomistic processes behind deformation of Tungsten at nanoscale. The

primary objective of the thesis is to observe the deformation behaviour of nanoscale tungsten, both single and polycrystal. Moreover, a comprehensive study on the parameters governing the creep of nanocrystalline tungsten in light of the Eq. 1.4 is also intended. Key objectives of the work can be mentioned in the following points:

- To conduct atomistic simulation of tensile test experiment on single crystal and polycrystalline tungsten to find out impact of temperature, diameter, and grain size on mechanical properties of Tungsten.
- To identify whether inverse Hall-Petch behavior is present in polycrystalline Tungsten. If present to identify the modified Hall-Petch equation describing the phenomenon.
- To delineate the atomistic processes of plasticity in single and polycrystalline Tungsten.
- To study the stress-, time-, temperature-, and grain size-dependent creep behavior in tungsten at nanoscale and identify the governing parameters controlling creep rate.
- To find the physical interpretation of the exponents of the Bird-Don-Mukherjee equation.
- To identify the diffusion controlling parameters during creep in nanocrystalline Tungsten.

## 1.10 Outline of the Thesis

Primary goal of the present work is to analyze the tensile deformation and creep mechanisms in nanocrystalline Tungsten. The thesis is structured so that before entering into the main analysis, a reader can get clear idea on the theoretical background and previous studies related to the topic. Chapter 1 is dedicated to describe the fundamental concepts of material deformation at the nanoscale especially bcc metals. The chapter also describes the previous studies on deformation and creep studies on different metals

using molecular dynamics and experiment. At the end the chapter delineates the major objectives of the study.

Chapter 2 outlines the numerical methods involved in solving the equation of atomistic simulation in brief. This chapter is focused on the concepts relevant to this work with detail idea on force-field parameters. Moreover, the chapter discusses the validation works performed for the study. Finally, the chapter describes the problems studied in this work. Physical description along with schematic diagrams are presented for both the problems. The chapter also describes the necessary boundary conditions used for the two parts of this work.

Results of analysis on single crystal and polycrystalline Tungsten nanowires are presented in chapter 3. Different physical properties including stress vs strain behaviour, Young's modulus, failure strain, etc. are observed for the nanowires. Moreover, with the help of atomistic visualization technique different stages of failure of nanowire are observed.

Chapter 4 deals with discussion of results for creep deformation in nanocrystalline Tungsten. It describes in detail the influence of different parameters of Eq. 1.4 on the physical processes behind the creep. Moreover, with the help atomistic simulation results, this chapter discusses the creep processes.

Finally, chapter 5 concludes and summarizes entire work by presenting key findings of the analysis.

# Chapter 2

## Simulation Methodology

This chapter deals with the numerical simulation procedure followed to solve problems the problems in the thesis. For convenience of the readers, this chapter introduces fundamentals of molecular dynamics method as prologue for the studies performed in this work. Later, physical details of the problems of both parts of the thesis are discussed. Validation of the numerical approach and justification of choosing inter-atomic potential to describe the interaction between the atoms are also provided in brief.

### 2.1 Molecular Dynamics

Recent advancements in computational algorithm and technology has made molecular dynamics a very popular mean of simulation at atomic-scale. This method was first introduced to analyze the thermodynamic properties of gases and liquids in 1960s [1]. The method became popular to solve the problems of mechanics in 1980s. Molecular dynamics (also known as “MD”) is a computational tool that describes the positions, velocities, and orientation of atoms as functions of time. During the calculations, this method assumes atoms as hard spheres or soft spheres and electrons are thought to be glued to the nuclei as depicted in Figure 2.1. By eliminating the electron’s degree of freedom, MD predicts the position of individual atoms using appropriate inter-atomic potential function. It is possible to take into account the electronic contribution to the

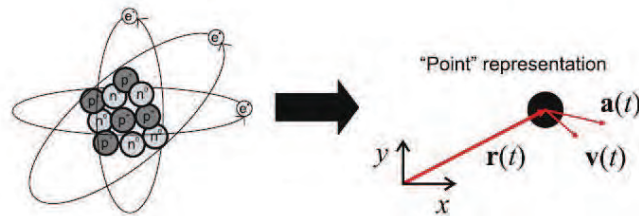


FIGURE 2.1: Assumption of molecular dynamics.

motion (*ab initio* analyses) but MD simulations provide some computational advantages [75].

### 2.1.1 Advantages of MD

Molecular dynamics simulation provides several computational advantages over many other continuum and *ab initio* simulation. Some of these are:

- The only input of MD is the positions of and interaction between the atoms. It directly solves the equations of motion to predict the future trajectories of the atoms.
- Unlike finite element method, MD involves no priori assumption about problem. As a result, new results can be found from MD simulation. This method can act as computational experiment.
- In the fields of nanomechanics, it is often required to know about the deformation mechanism like dislocation or twinning. It is not possible if the simulation is done under the continuum assumption.
- MD simulation can provide important guidelines for multi-scale modeling.
- Stress singularities like stresses at the crack tips are handled naturally unlike continuum methods.
- MD can simulate mechanics problems at a high strain rate inaccessible by the continuum methods.

## 2.1.2 Disadvantages of MD

Although classical molecular dynamics is an extensively used computational tool it has some disadvantages too. Some of the most prominent downsides are:

- \* One of the most severe limitations of the classical MD methods is the length- and time-scale it deals with. In order to predict average properties of a macroscopic system, the resolution of the time-step in classical MD needs to be around  $10^{-15}$ s. This seriously limits the application of this method as simple microsecond scale simulation may take several months to complete [1]. Moreover, the length-scale is in the nanometer range ( $10^{-9}$  m). As a result, most of the times it is not possible to infer bulk properties from the molecular dynamics simulation. Number of atoms involved in the simulation directly dictates the time required to solve a problem. This makes simulations involving multi-million atoms not feasible in most cases.
- \* In order to completely define optical properties, magnetic properties and even thermal properties of materials one needs to take into account the electronic contribution. While DFT can perform such calculation albeit in small systems, classical molecular dynamics ignores the electronic contributions to measure physical properties [1, 76].

## 2.2 Steps of MD Simulation

The basic steps of classical molecular dynamics is presented in brief manner in Figure 2.2. One can enlist these steps as [1, 76],

- a. Define the system of particles at the beginning of the simulation. This definition includes position and velocities of the particles at a specific time.
- b. Obtain expression of force using appropriate potential function.
- c. Minimize the energy of the structure.
- d. Solve Newton's equation of motion.

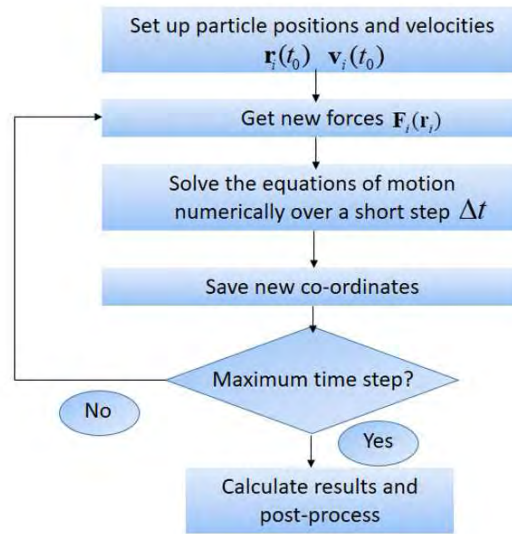


FIGURE 2.2: Steps to solve molecular dynamics simulation.

- e. Update the positions and velocities of the atoms in the system for incremental time-step  $\delta t$ .
- f. Analyze data using statistical methods.

In the following sections each of these steps will be briefly discussed and their implementation in this work will be highlighted.

### 2.2.1 Initialization

In order to calculate the positions and velocities of the atoms at a future instant one needs to define the initial positions of the atoms at first. Normally, one needs to define crystal structure and co-ordinates of the atoms in the system. In case of nanowires, one needs to mention the radius of the nanowire and orientation of the crystal structure along the co-ordinate axes. However, the initialization may require more information in case semi-quantum forcefields like ReaxFF [77]. In such forcefields one needs to mention the charge of the particles too. In other forcefields the bond angles may need to be mentioned.

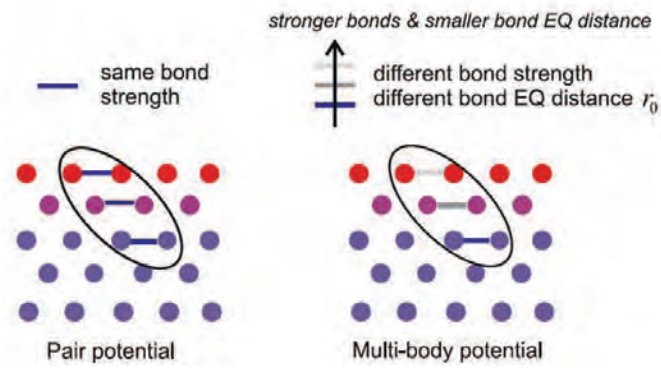


FIGURE 2.3: Comparison between pair potential and multi-body potential.

## 2.2.2 Force field

The most important component of molecular dynamics calculation is the force field or *potential*. It describes how atoms in molecular dynamics simulation interact with each other. There are a number of inter-atomic potentials or force fields. Choice of one particular force field depends on the type of materials, nature of the problem, computational facilities, etc. In order to understand how force is calculated in MD simulation, one needs to understand how the force field or potential works. The total energy of the system,  $U_{total}$  is approximated by the summation of energy for all atomic bonds in the system. For example if the system has  $N$  atoms the total energy of the system can be defined as,

$$U_{total} = \frac{1}{2} \sum_{i \neq j=1}^N \sum_{j=1}^N \phi(r_{ij}). \quad (2.1)$$

Here  $r_{i,j}$  is the distance between particles  $i$  and  $j$  and  $\phi$  is the potential energy acting between an atom and its neighbours. The  $\frac{1}{2}$  at the front shuns the double counting of the bonds. The key part of the any force field is the definition of  $\phi$ . The definition must include both repulsive and attractive contributions of the atomic potential. There are two ways to define  $\phi$ -

- **Pair potential:** This is the simplest way of describing interaction between atoms. One such potential is Lennard-Jones (LJ) potential. It does not consider complex terms like bond angle, electron density, etc. in its definition. Still it is a very



good potential to calculate problems involving gases and liquids [78, 79]. It can also explain complex calculation involving  $SiO_2$ . The LJ potential can be fitted to calculate the elastic constants of many metals [1] but it is not appropriate for most metals.

- **Multi-body potentials:** Oversimplification in the description of interaction in the pair potentials leads to significant errors. For example, interaction between the atoms is not the same for atoms inside a bulk material and atoms at the surface as shown in Figure 2.3. This difference is not addressed in the pair potentials. Multi-body potentials solve this problem by considering the bond energy between atoms not as function of only distance but also positions of all other atoms at the vicinity of that atom [1]. Local environment thus plays a vital role in such potentials. In case of metals, the most commonly used many-body potential is the Embedded Atom Method (EAM) potential. EAM potentials have been successfully used to describe the behaviour of many pure metals like *Ni*, *Cu*, and *Al* and their alloys [1]. In this work, modified EAM potential for Tungsten is used for both nanowire and creep analyses.

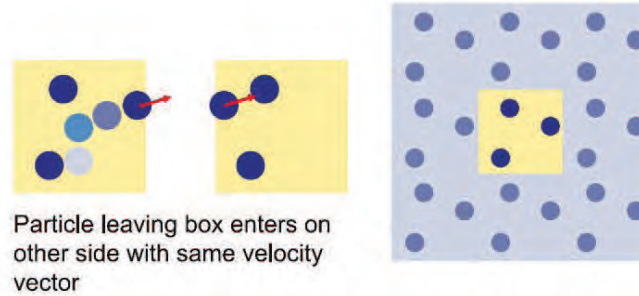


FIGURE 2.4: The figure shows how periodic boundary condition works.

### 2.2.3 EAM Potential

EAM potential has many different version. However, all of these have a general expression for potential which is,

$$U_i = \sum_{j=1}^{N_i} \phi(r_{ij}) + f(\rho_i). \quad (2.2)$$

Here  $\rho_i$  is the local density of electron and  $f$  is the embedding function [1]. The term  $\rho$  describes the local environment of an atom while  $f$  explains how energy of atom depends on local energy density. Therefore, one can see that multi-body potentials like EAM consists of a term like LJ potential and correction for local environment. Moreover, these are semi-empirical potentials. This means that the function  $f$  is based on fitting parameters. As a result, these potentials can describe many defects in solids in much better way [1]. However, most multi-body potentials are not capable of considering the effect of directional bondings. To address this problem modified EAM (MEAM) potentials are proposed.

### 2.2.4 Force Calculation

From the total potential energy of the system the forces acting on each particle can be calculated. It is known to us that the force is negative gradient of the potential energy in any potential force field. From this relationship we can write that,

$$\vec{F}_i = -\frac{dU}{d\vec{r}_i} \quad (2.3)$$

where  $\vec{F}_i$  is the force acting on  $i^{th}$  atom. Now from Newton's second law of motion one can write for an atom with mass  $m_i$  that,

$$m_i \frac{d^2 \vec{r}_i}{dt^2} = -\frac{dU}{d\vec{r}_i}. \quad (2.4)$$

For the entire system Eqn. 2.4 refers to a system of coupled second-order nonlinear differential equations. These equations are solved numerically using finite difference algorithm. Time integration of these equation involves a simple strategy. One can update the positions of all the atoms using previous co-ordinates by using Taylor expansion of the position vector  $\vec{r}_i$  [1],

$$\vec{r}_i(t_0 + \delta t) = \vec{r}_i(t_0) + \vec{v}_i(t_0)\delta t + \frac{1}{2}\vec{a}_i(t_0)\delta t^2 + \dots \quad (2.5)$$

and

$$\vec{r}_i(t_0 - \delta t) = \vec{r}_i(t_0) - \vec{v}_i(t_0)\delta t + \frac{1}{2}\vec{a}_i(t)\delta t^2 + \dots \quad (2.6)$$

Adding Eqns. 2.5 and 2.6 we get,

$$\vec{r}_i(t_0 + \delta t) = -\vec{r}_i(t_0 - \delta t) + 2\vec{r}_i(t_0) + \vec{a}_i(t)\delta t^2 + \dots \quad (2.7)$$

The accelerations can be calculated by,

$$\vec{a}_i = \frac{\vec{F}_i}{m} \quad (2.8)$$

The updating scheme mentioned here is known as Verlet central difference method [1]. In this thesis for time integration velocity Verlet algorithm has been used. In this scheme positions are updated as mentioned above while velocity is updated as,

$$\vec{v}(t + \delta t) = \vec{v}_i(t) + \frac{1}{2}(\vec{a}_i(t) + \vec{a}_i(t + \delta t))\delta t. \quad (2.9)$$

### 2.2.5 Energy Minimization

Energy minimization is performed in any molecular simulation in order to get the most stable structure. It is known that the most stable system occurs when it reaches the lowest energy state. In order to find the most stable system or optimized geometry energy minimization is performed in this work using conjugate-gradient algorithm [80].

### 2.2.6 Boundary Conditions

Boundary conditions are employed in molecular dynamics simulations to solve the equations of motion. These boundary conditions should reflect the physical constraints of computational experiments performed in the simulation. There can be different boundary conditions like fixed or rigid boundary, semi-rigid boundary, periodic boundary, etc [75]. In this thesis, for the work of creep simulation periodic boundary condition

is used along the directional axes. However, in case of nanowire simulation, periodic boundary condition is employed only along the nanowire axis. On the other two axes, free surface boundary condition is assumed. Before going into detail of justifications of such boundary condition, it will be helpful for the readers to review the basic concepts of periodic boundary condition.

Periodic boundaries mimic infinite boundaries of a bulk material. That means it assumes that all the particles in a system are connected. It enables us to calculate the bulk properties of a material using small number of particles. Figure 2.4 shows an implication of periodic boundary condition. Under this boundary condition, if an atom moves out of the simulation box in one direction it re-enters from the opposite direction with same velocity. The primary cell is assumed to be repeated in all the directions and all the particles inside the primary cell always have same momenta.

In case of creep simulation, the simulation box is taken as a representative of the larger system. It essentially mimics the bulk system. Therefore, periodic boundary condition is the right choice for the system. However, in case of nanowire simulation, because of the surface stress caused by the atoms on the surface of the nanowires, perfect periodic boundary condition creates a hindrance. It shows artificial stress values. As a result, one needs to consider the surface of the nanowire as free surface. On the other hand, the lengthwise direction of a nanowire must mimic the bulk as uniaxial tensile tests are used to predict bulk behaviour. For these reasons, in case of nanowires' simulation, periodic boundary condition is used only along the lengthwise direction.

## 2.3 Statistical Ensembles

In order to control temperature and pressure inside the different statistical ensembles can be employed in molecular dynamics simulations. These ensembles include  $NPT$ ,  $NVE$ ,  $NPH$ ,  $NVT$ , and  $\mu PT$  ensembles [75].

- $NVE$  ensemble deals with constant number of atoms, volume, and energy. This is also known as micro-canonical ensemble of isolated system. In this work  $NVE$  ensemble used along with thermostat to reach a desired temperature.

- *NPT* ensemble has constant number of atoms, pressure, and temperature. *NPT* ensemble is used to equilibrate a system to a certain temperature and pressure.
- *NVT* ensemble keeps the number of atoms, volume, and temperature of a system constant.
- *NPH* is a constant atom, pressure, and enthalpy ensemble.
- $\mu PT$  is a grand canonical ensemble which has constant chemical potential, pressure, and temperature.

## 2.4 Physical Modeling

### 2.4.1 Tungsten Nanowire

#### 2.4.1.1 Single Crystal

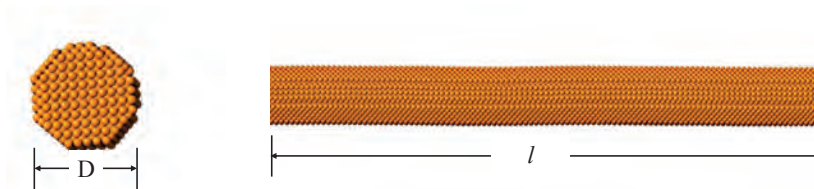


FIGURE 2.5: Schematic diagram of the single crystal Tungsten nanowire with length  $L$  and diameter  $D$ .

Figure 2.5 shows the schematic diagram of the single crystal Tungsten nanowire considered in this work. In this figure, the diameter of the nanowire is denoted by  $D$  and length by  $L$ . The atoms are in perfect bcc crystal structure. The nanowire is placed along the  $X$  axis while the cross-section of the nanowire is in the  $YZ$  plane. Periodic boundary condition is assumed along the  $X$  axis and free surface is considered as the wire surface. These boundary conditions mimic the actual nanowire under loading.

### 2.4.1.2 Polycrystalline

Polycrystalline  $W$  nanowire for this work is built with randomly oriented grains. Polycrystals are created using Voronoi tessellation [81] method with Atomsk tool [82]. Initially, a rectangular box is created with desired average grain size and later nanowires of required size are cut from it. In Figure 2.6 (b),  $D$  and  $l$  stand for the diameter and length of the nanowire, respectively. Just like the single crystal nanowire, periodic boundary condition is applied along the axis of the nanowire keeping the wire surface stress-free. Number of atoms for simulation is varied depending on the condition from 3897 to 61295.

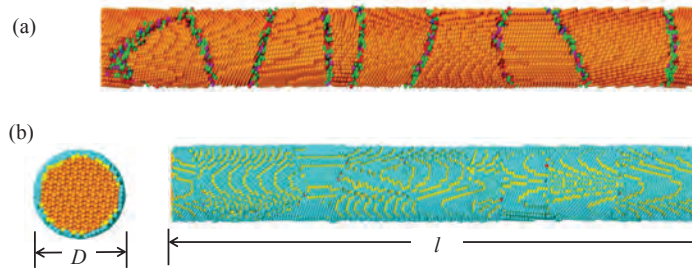


FIGURE 2.6: Schematic diagram of the (a) sample nanowire and (b) diameter and length of sample nanowire.

## 2.5 Creep Analysis Model

In order to analyze creep at nanoscale a polycrystalline cubic sample of  $W$  is created by Voronoi tessellation method [81] using Atomsk tool [82] with randomly oriented grains of 2.38 nm, 2.86 nm, 3.57 nm, and 4.76 nm size is considered. The dimensions of the cubic sample is taken as 14.27 nm  $\times$  14.27 nm  $\times$  14.27 nm for every grain size totaling to number of atoms ranging from 180,437 to 181,208. Figure 2.7 shows the initial sample after preparation. Periodic boundary condition is imposed in all the three directions to mimic a small sample of large bulk material.

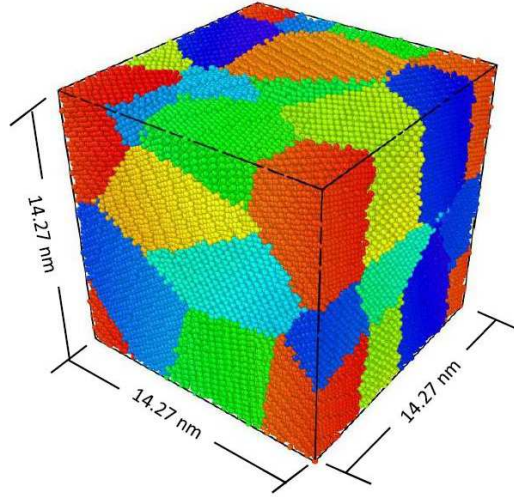


FIGURE 2.7: Schematic diagram of the cubic sample of tungsten nano-crystal with dimensions.

## 2.6 Calculation of Physical Properties

### 2.6.1 Stress

The stress is calculated using a modified form of virial theorem. The original form of the virial theorem suggests that for any pair potential  $V$ , the equation of stress stands as [83],

$$\sigma_{ij} = \frac{1}{\Omega_{Tot}} \sum_{\alpha=1,n} \left( \frac{1}{2} m^{\alpha} v_i^{\alpha} v_j^{\alpha} + \sum_{\beta=1,n} \frac{r_{\alpha\beta}^i r_{\alpha\beta}^j}{|r_{\alpha\beta}|} \frac{dU}{dr_{\alpha\beta}} \right). \quad (2.10)$$

Here  $i, j$  denote the indices in Cartesian coordinate system while  $\alpha$  and  $\beta$  are the atomic indices.  $\Omega_{Tot}$  denotes the total volume of nanowire and  $m^{\alpha}$  and  $v^{\alpha}$  are respectively the mass and velocity of atom  $\alpha$ .  $r_{\alpha\beta}$  is the distance between atoms  $\alpha$  and  $\beta$ . The term  $\frac{dU}{dr_{\alpha\beta}}$  denotes the scalar of the force exerted by atom  $\beta$  on atom  $\alpha$ . Zhou [84] definitively proved that inclusion of the kinetic term (first term in the right hand side of Eqn. 2.10) erroneously calculates the stress and hence in this study kinetic contribution of the atoms to stress is neglected.

### 2.6.2 Mean Square Displacement (MSD)

Diffusive properties of  $W$  nanocrystal is measured in this work while deciphering the creep mechanism using mean square displacement (MSD) defined as [85],

$$MSD = \left\langle \frac{1}{N} \sum_{i=0}^N (r_i(t) - r_i(0))^2 \right\rangle. \quad (2.11)$$

Here,  $N$  is the particle number,  $t$  is time, and  $r_i(t) - r_i(0)$  is the distance traveled by a specific particle over the time at different constant temperatures.

### 2.6.3 Pressure and Temperature

The pressure is calculated by [1]

$$P = Nk_B T - \frac{1}{3} \frac{1}{V} \sum_{i=1}^N \sum_{j=1, j < i}^N \left\langle r_{ij} \frac{d\phi}{dr_{ij}} \right\rangle \quad (2.12)$$

Here,  $k_B$  is Boltzmann's constant.

Temperature of the system is calculated using the following relation,

$$T = \frac{2 \langle K \rangle}{3 N k_B} \quad (2.13)$$

where  $K$  is the kinetic energy of the system.

### 2.6.4 Strain

In case of nanowires, strain is calculated using the following relation,

$$\epsilon = \frac{l - l_0}{l_0}, \quad (2.14)$$



where  $l$  is the instantaneous length of the nanowire under tension and  $l_0$  is the undeformed length of the nanowire.

## 2.7 Validation of Potential

In order to perform atomistic simulation with sufficient accuracy both EAM and MEAM potentials were tried. However, for the entire work a modified embedded atom (EAM) potential by Zhou et al. [86] is used. This potential was successfully used in previous work of B. Ma et al. [50]. The potential could successfully reproduce the cohesive energy of  $-8.76$  eV and lattice constant of  $3.17 \text{ \AA}$  [87] for single crystal  $W$ . On the other hand, MEAM potential failed to predict the vacancy formation energy. Moreover, it also failed to show the twinning deformation for single crystal Tungsten similar to the works of Wang et al. [49]. Finally, this potential could successfully reproduce the melting point of nanocrystalline  $W$  as  $4000$  K which is close to that of  $3900$  K of Moitra et al. [88] as shown in Figure 2.8.

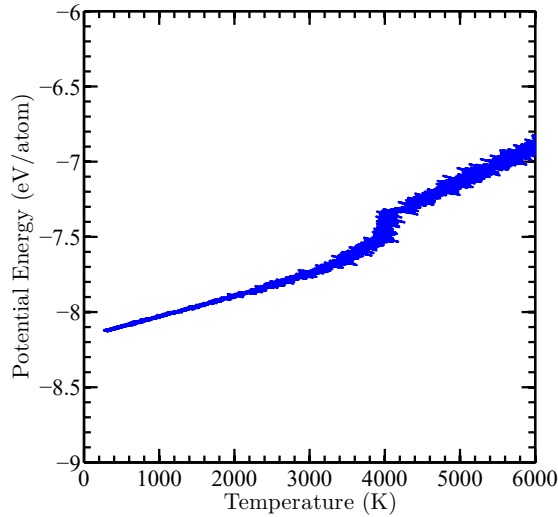


FIGURE 2.8: Variation of potential energy per atom with temperature using EAM potential of this work.

## 2.8 Simulation and Visualization

For both parts of this thesis, molecular simulations are carried out in Large-scale Atomic/Molecular Massively Parallel Simulator (LAMMPS) [89]. Visualization of atomistic deformation processes is done by OVITO [90] and AtomViewer software [91]. Dislocation processes are analyzed by DXA [92] algorithm. In case of uniaxial tests of nanowires before applying tensile load the energy of the system is minimized using conjugate gradient algorithm. After that *NVT* and *NPT* simulations are carried out to ensure desired temperature and zero pressure in all directions. Finally the box is deformed at a fixed strain rate of  $10^9 \text{ s}^{-1}$ . The uniaxial deformation is performed under *NVT* ensemble to control temperature fluctuations. A constant integration time step of 1 fs is used during all the simulations.

Since attaining actual creep rate in atomistic simulation is beyond the scope of computational facilities used for this work, high values for applied stress and temperature are considered to simulate creep mechanism within nanoseconds duration. For creep simulations, before applying external stress, the structure is minimized using conjugate gradient method with time step of 0.001 ps. Then the structure is equilibrated at a certain temperature using *NPT* ensemble for 200 ps. Finally, a constant tensile stress is applied along x-direction while keeping other directions stress-free for another 200 ps.

## 2.9 Summary

Goal of this chapter is to introduce the numerical simulation methodology and physical details of the problems discussed in this work. By briefly discussing the background of molecular dynamics simulation and validation of potential used, the propriety of current simulation is established. Synergistic discussion of both physical and numerical aspect of the problem should help the readers to understand the discussions on the results in the later chapters.

# Chapter 3

## Tensile Behavior of *W*

### 3.1 Introduction

This chapter deals with the first part of the entire thesis. In this part, the deformation behaviours of single and polycrystalline nanowires are discussed. Deformation mechanism in bcc nanowires has been a major topic of research to the materials scientists. Debate over the prevailing plasticity mechanism has made it imperative to conduct a thorough study on the factor governing plasticity and failure in bcc nanowire. In this chapter major factors governing plasticity in single and polycrystalline Tungsten nanowires have been investigated including effects of temperature, diameter, loading direction, grain size, etc.

### 3.2 Single Crystal Nanowire

The primary goal of investigation in case of single crystal Tungsten nanowire is to observe the mode of deformation (twinning or dislocation, brittle or ductile, etc.), effect of temperature, diameter and crystal orientation on strength and failure mechanism. For this study, nanowires of diameter 2 nm, 3 nm, 4 nm, and 5 nm are taken. Temperatures are taken as 10 K, 100 K, 300 K, 500 K, and 1000 K for single crystal nanowires. Furthermore, the crystal orientations considered are  $\langle 100 \rangle$ ,  $\langle 102 \rangle$ ,  $\langle 110 \rangle$ ,  $\langle 111 \rangle$ , and

$\langle 112 \rangle$ . In order to avoid the effect of nanowire length on the mechanical properties, aspect ratio or length to diameter ratio is kept 1:10 for each case.

### 3.2.1 Effect of Temperature

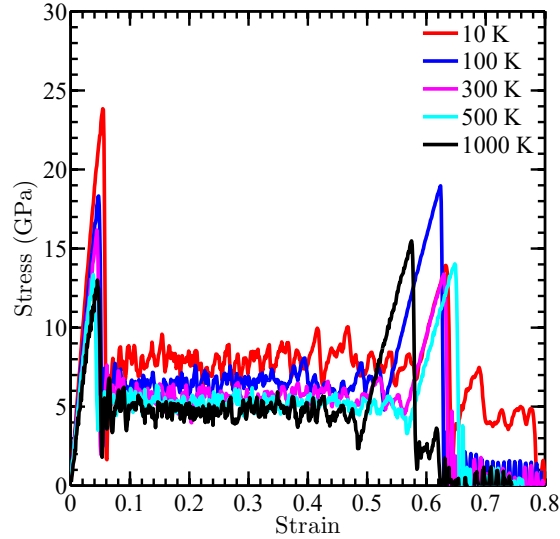


FIGURE 3.1: Stress vs strain diagram for single crystal Tungsten nanowires of 2 nm diameter at different temperatures.

Tensile stress vs strain curves for  $\langle 100 \rangle$  oriented 2 nm diameter Tungsten nanowires at different temperatures are shown in Figure 3.1. In this figure, one can see that at different temperatures, the stress-strain behaviour does not change dramatically. All the cases show some common features. Computed stress shows a characteristic linear elastic region with strain up to a certain portion. After application of a certain strain, the nanowire yields but does not rupture. An abrupt fall in stress value occurs. Further tensile load causes oscillation of stress at a particular value. This region occurs due to twins' propagation which will be discussed later. Interestingly, after application of further strain, there is a stress surge just before the rupture of nanowire. A secondary peak in stress occurs and the nanowire fails. The entire stress vs strain behaviour shows evidence of ductile failure and similar has been reported in other works regarding Tungsten nanowire [49, 50]. The value of this secondary peak of stress actually varies. It is observed that for lower temperatures, this secondary peak stress is lower than the yield point [50]. However, in this analysis, it is observed that for 300 K temperature, the secondary stress is lower than the yield point at that temperature while for 100 K it

is higher than the yield point at that temperature. Therefore, the previous claim seems inconclusive. In the coming sections, it will be explained why only temperature can not be the deemed as the primary reason for this stress surge.

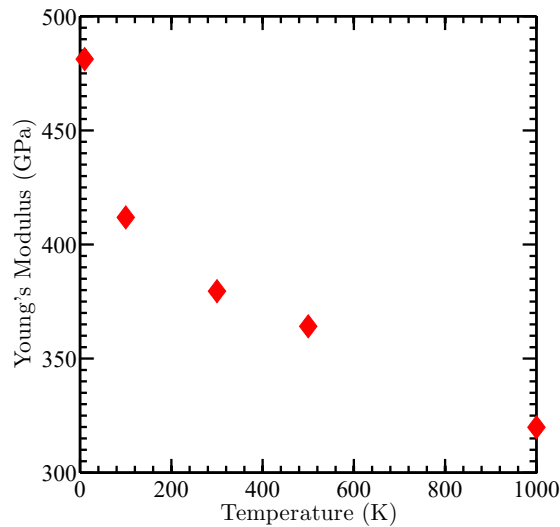


FIGURE 3.2: Variation of Young's modulus with temperature for single crystal Tungsten nanowire of 2 nm diameter.

In order to explore the impact of temperature on the strength and stiffness of the nanowire, Young's moduli (Figure 3.2) and yield strength (Figure 3.3) of the nanowires are measured as function of the temperature for a nanowire of 2 nm diameter. Both of these properties show similarities in their variation with the temperature. One can see from Figure 3.2 that the Young's modulus of the single crystal tungsten nanowire decreases as the temperature is raised. This means the wires become less stiff at elevated temperatures. This is an expected conclusion as one can understand that elevated temperature provides higher energy to the atoms of the nanowire. Similar physical reasoning can also be made for the yield strength of the nanowires. Detail physical mechanism behind the failure process will be elucidated in the section §3.2.4.

### 3.2.2 Effect of Diameter

Next venture of this work is to find whether the phrase "Smaller is stronger" is true in case of single crystal Tungsten nanowire. In order to test this, nanowires of 2 nm, 3 nm, 4 nm, and 5 nm diameters are taken and uniaxial tensile tests have been performed on

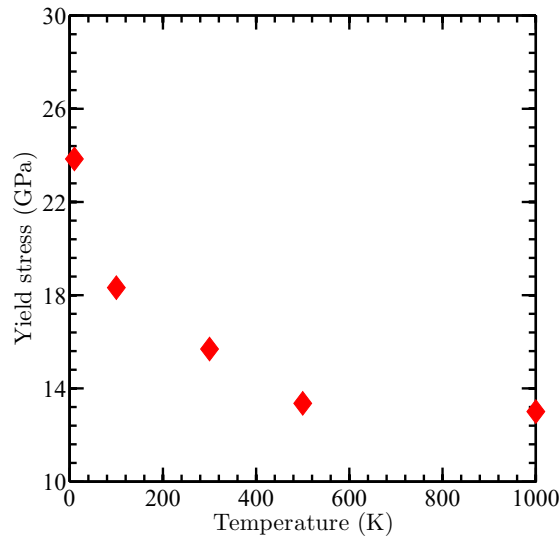


FIGURE 3.3: Variation of yield stress with temperature for single crystal Tungsten nanowire of 2 nm diameter.

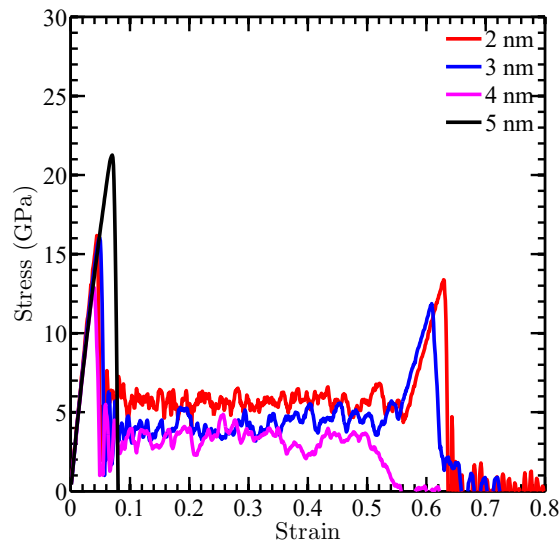


FIGURE 3.4: Stress vs strain diagram for single crystal Tungsten nanowires of different diameters at 300 K temperature.

those nanowire at a temperature of 300 K. The corresponding stress vs strain diagram has been shown in the Figure 3.4. The diagram shown an astounding feature of Tungsten nanowire. It is known that bulk Tungsten is a brittle material at room temperature. However, both experimental works and simulations have shown that nanocrystalline Tungsten is ductile at room temperature. Trace of the ductile behaviour is found in nanowires of 2 nm, 3 nm and 4 nm diameters where one can see that the failure mechanism clearly shows double-peaks in the stress vs strain diagram. The first peak indicate

the first yield point where deformation twins generate. The propagation of twin is manifested in constant stress section of the stress vs strain diagram. However, if one takes a closer look at the diagram, the nanowire with 5 nm diameter fails suddenly by rupture. Not only that, it also violates the so called “Smaller is stronger” rule having the highest yield point among the structures considered. Moreover, the failure is sudden and there is no double-peak in the stress vs strain diagram. This shows that as the dimension of single crystal tungsten nanowire approaches its bulk counterpart, it begins to show brittle fracture.

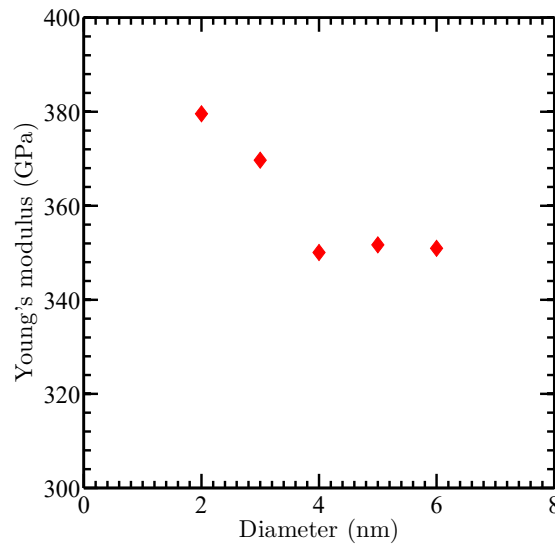


FIGURE 3.5: Variation of Young's modulus with diameters for single crystal Tungsten nanowire at 300 K temperature.

Figure 3.5 shows the variation of Young's modulus with diameters. In this figure it can be seen that as the diameter of the nanowire is increased, the stiffness has decreased. The stiffness of 5 nm diameter nanowire increased ever so slightly. This result posits that though the failure mechanism and yield strength of the nanowire with 5 nm diameter reflects brittle fracture, the stiffness is not affected a great deal. It can be explained by the fact that the ductile failure mechanism of nanowires is purely deformation twin based. However, before twins generate, the tensile force acts on the atoms in a similar fashion for all the nanowires considered. Therefore, it is expected that stiffness would not be impacted by the failure mechanism that much. Bulk Tungsten also shows stiffness of the same order of magnitude. However, the yield stress shows a meteoric rise in case of 5 nm diameter (see Figure 3.6). However, if the diameter of the nanowire is increased to a value of 6 nm, it begins to weaken compared to the 5 nm diameter nanowire. It

proves that the jump in the strength is due to the shift in failure mechanism. Nanowires with higher diameters are tested and it is seen that nanowires with diameter 5 nm or more fails in brittle manner. So it can be inferred that diameter of the nanowire serves as important factor that can change the failure mechanism of the nanowire.

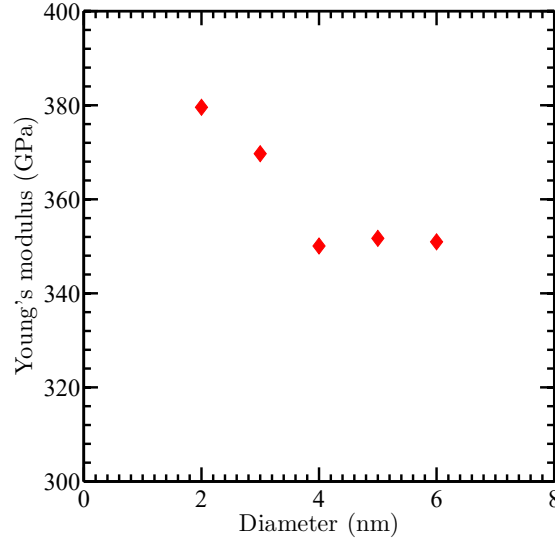


FIGURE 3.6: Variation of yield stress with diameters for single crystal Tungsten nanowire at 300 K temperature.

### 3.2.3 Effect of Crystal Orientation

Since one of the major objectives of the thesis is to explore the impact of grains and grain boundaries on the mechanical properties of the Tungsten nanowire it seems appropriate to study the impact of loading orientation on the mechanical properties of single crystal nanowire. To do so, nanowires of 2 nm diameters are taken and tensile load has been applied along five crystal orientations namely  $\langle 100 \rangle$ ,  $\langle 102 \rangle$ ,  $\langle 110 \rangle$ ,  $\langle 111 \rangle$ , and  $\langle 112 \rangle$  at 300 K temperature. The stress vs strain diagram of the computational experiment has been shown in Figure 3.7. The diagram shows an interesting pattern. While only  $\langle 100 \rangle$  and  $\langle 102 \rangle$  loadings show ductile behaviour other orientations clearly depicts brittle fracture. Moreover, each crystal orientation differs in their stiffness and yield stress too (see Table 3.1). This is not the first time this effect is observed. Previous studies also showed that loading orientation leaves a huge impact on the mechanical properties of nanowire [43, 93]. In the Figure 3.7, it is evident that initial elastic deformation is maximum in case of loading along  $\langle 111 \rangle$  direction while minimum along



Crystal orientation	Young's modulus (GPa)	Yield strength (GPa)
$\langle 100 \rangle$	379.56	16.17
$\langle 102 \rangle$	349.29	13.28
$\langle 110 \rangle$	340.67	24.29
$\langle 111 \rangle$	358.75	39.04
$\langle 112 \rangle$	340.83	22.89

TABLE 3.1: Young's modulus and yield stress of nanowires with 2 nm diameter at different crystal orientations.

$\langle 102 \rangle$  and  $\langle 100 \rangle$  directions. Physical reasoning behind such incident can be provided by the surface energy of the crystal structure. Along the  $\langle 111 \rangle$  direction the atoms of Tungsten has the lowest surface energy and hence the most stable structure. This makes the structure stronger and it becomes able to resist higher load.

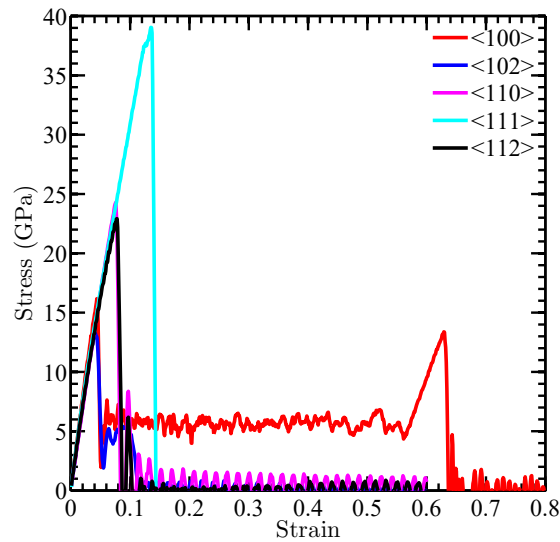


FIGURE 3.7: Results for loading along different crystal orientations at 300 K temperatures and 2 nm diameter.

In case of Young's modulus, one can observe in Table 3.1 that it is the highest for loading along the  $\langle 100 \rangle$  direction. On the other hand, it is the lowest for loading along  $\langle 110 \rangle$  direction. It is noticeable that the Young's modulus jumps slightly for loading along  $\langle 111 \rangle$  direction.

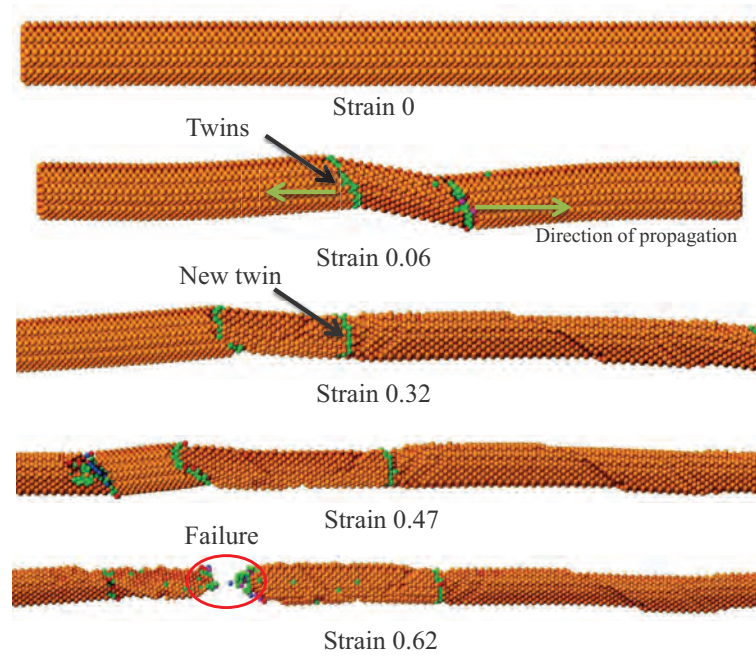


FIGURE 3.8: Atomistic configurations of nanowire of 3 nm diameter at 300 K at different stages of uniaxial tensile test.

### 3.2.4 Failure Mechanism

In order to explore the mechanism of failure during uniaxial tensile test performed in the work, plastic deformation in nanowires of 3 nm and 4 nm diameters are observed. Figure 3.8 shows atomistic pictures of plastic deformation in the single crystal nanowire of 3 nm diameter under applied loading along the  $\langle 100 \rangle$  direction. Snapshots are shown for 0%, 6%, 32%, 47%, and 62% strains. At 6% strain emergence of  $\{112\}$  twin boundaries in the nanowire can be observed. The twin boundaries contain  $\frac{1}{6} \langle 111 \rangle$  twinning partial dislocation. By repeated nucleation of  $\frac{1}{6} \langle 111 \rangle$  dislocation the twins glide along the nanowire's axis. First emergence of this twin is manifested as the yield point. As the applied strain is raised the twin boundaries travel in the opposite direction along the nanowire. Now in the rotated crystal in between the twin boundaries repeated slip occurs and this manifests itself as fluctuating flow stress (constant stress in stress vs strain diagram). A second peak or the hardening region occurs because now the rotated crystal acts like a newly oriented nanowire. Hence, the required stress for rupture becomes higher. Finally, at 62% strain one can see sudden rupture of the nanowire.

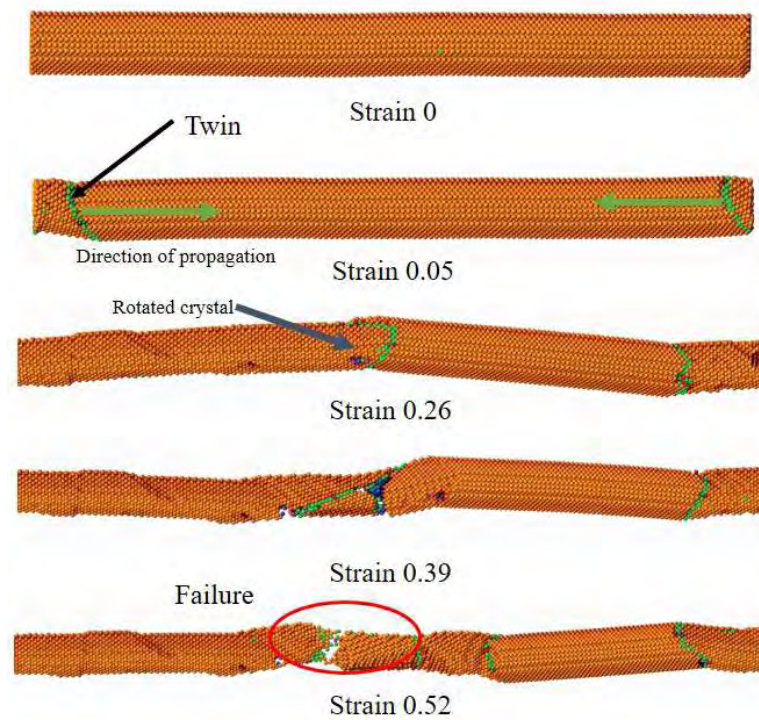


FIGURE 3.9: Atomistic configurations of nanowire of 4 nm diameter at 300 K at different stages of uniaxial tensile test.

In Figure 3.9, similar presentation of atomistic pictures for single crystal nanowire of 4 nm diameter are shown. In this figure, the twin generates at about 5% strain and propagates inwards. Along the nanowire's axis the box is considered periodic. Hence, the reorientation of crystal can be understood as explained for nanowire of 3 nm diameter. It is observed from Figure 3.4 that in case of 4 nm diameter nanowire, there is no second peak. This occurs because this time, at 39% strain the failure does not occur from re-oriented crystal rather it occurs from twin plane. That is why the second stress peak is not visible. Finally the complete rupture occurs at 52% strain.

To get an idea about the brittle failure mechanism in the single crystal nanowire along  $\langle 111 \rangle$  direction, single crystal nanowire of 2 nm diameter is observed to study the failure mechanism. In contrast to the ductile mode of deformation, along the  $\langle 111 \rangle$  direction the nanowire fails in brittle manner. This occurs because energetically favourable plane for  $\frac{1}{6} \langle 111 \rangle$  twin deformation is 112 planes. However, if the loading is applied along  $\langle 111 \rangle$  direction it is not possible for twins to grow and propagate along 112 planes. In Figure 3.10, snapshot at the moment of rupture of a 2 nm diameter nanowire is shown.

Here one can observe that instead of twin deformation necking and subsequent failure has occurred in this case.



FIGURE 3.10: Atomistic configurations of nanowire of 2 nm diameter at 300 K for loading at  $\langle 111 \rangle$  direction during uniaxial tensile test.

### 3.3 Polycrystalline Nanowire

The objectives of studying polycrystalline nanowires is to find the impact of grain size, external diameter, and temperature on the failure of polycrystalline Tungsten nanowire. Additionally, detecting the presence and nature of inverse Hall-Petch effect in deformation of polycrystalline nanowire is another important objective of the work. In order to find the impact of grain size on the elastic properties of the polycrystalline nanowire, a nanowire with diameter of 5 nm is taken with different average grain sizes (ranging from 4.63 nm to 25 nm) and uniaxial tensile test is performed at a temperature of 10 K. To study the impact of external size factor, the diameter of the nanowire is varied from 2 nm to 5 nm keeping average grain size constant at 6.79 nm at 10 K for uniaxial tension tests. Since length of the nanowire is a key governing parameter to determine failure mechanisms for different diameters, aspect ratio or length to diameter ratio is kept constant at 10. Finally, to study the effect of temperature, a polycrystalline nanowire with diameter 5 nm is considered with average grain size 6.79 nm and temperature is varied from 10 K to 500 K. The results are analyzed in terms of stress vs strain curves, Young's modulus, and yield stress. To observe the impact of the different factors on ductility of the nanowire, modulus of resilience is also considered. Finally, the fracture mechanism is discussed in detail in reference to the simulation.

#### 3.3.1 Impact of Grain Size

To elucidate that relationship between grain size and strength, the stress vs strain curves for a 5 nm diameter nanowire with different grain sizes at a constant temperature 10

K are presented in Figure 3.11 (a). Figure 3.11 (b) exhibits variation of Young's modulus of nanowire for different grain sizes. From Figure 3.11 it can be seen that there are two types of responses in stress with strain. The stress either shows double peaks depicting strain hardening or it shows a single peak and then gradual oscillating and descending trend with increasing strain. The strain hardening behaviour in single crystal *W* is observed in previous works too [50]. In those works only double peaks in the stress vs strain curve were found for each applied tensile strain. However, in this work, continuous flow of material is observed in some cases. The difference in the pattern is due to the change or shift in fracture mechanism. The root cause of the double peak in stress-strain curve is the interaction between twin and grain boundary. Because of impediment imposed by the grain boundary in the course of twin's motion, there is local stress concentration around grain boundaries. This manifests itself in the form of secondary peak in the stress-strain plot. There is actually a competition between two fracture modes-twinning dominant and grain boundary sliding. When grain boundary sliding becomes the dictating fracture mechanism double peaks are not there. Rather an oscillating response in the stress is observed as the strain is increased. Hence, occurrence of a double peak depends on whether the deformation twin interact with the grain boundary or not. In this work, for grain sizes of 14.91 nm and 6.79 nm distinct double peaks can be observed showing intense grain boundary-twin interaction. Figure 3.11 (b) shows variation of Young's modulus with grain sizes for 5 nm nanowire at 10 K. From this figure it can be observed that reducing the grain size actually reduces the Young's modulus of the nanowire below the grain size of 16.67 nm. It implies that the stiffness of the polycrystalline metal nanowire actually reduces as the size of the grains becomes smaller than a particular grain size. To illustrate this fact even further Figure 3.12 (a) can be discussed. This figure suggests that the common notion of smaller is stronger does not hold true below a critical grain size. Interestingly, the inverse relation of yield strength with grain size follows a linear relationship with inverse of the square root of the grain size just like Eqn. 1.3. However, the slope of Eqn. 1.3,  $k$ , has a negative value in this case. By linear fitting of data, this value is found to be 9.3945 while  $\sigma_0$  is 14.33 GPa. So inverse Hall-Petch relation for polycrystalline *W* nanowire can be written as,

$$\sigma_y = 14.33 - \frac{9.3945}{d^{0.5}}, \quad (3.1)$$

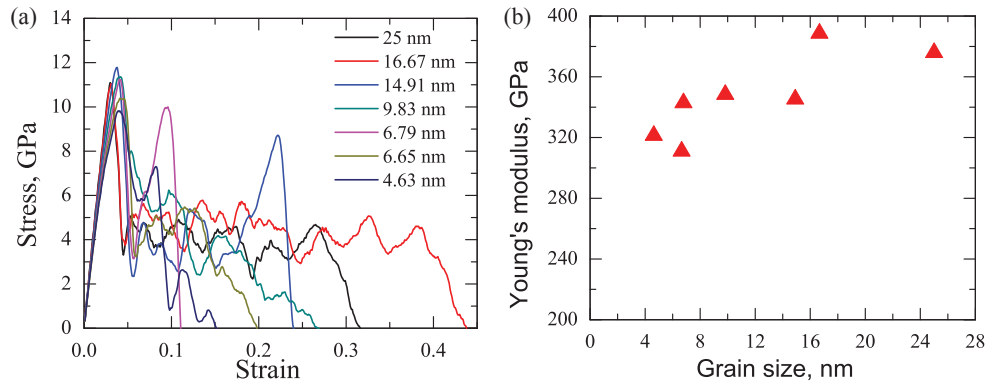


FIGURE 3.11: (a) Stress vs strain plot, and (b) Variation of Young's modulus for different grain sizes at 10 K temperature and for 5 nm diameter nanowire.

where  $\sigma_y$  is expressed in GPa and grain size in nm.

Figure 3.12 suggests that below critical grain size of 14.91 nm, the strength of nanowire actually decreases with further grain refinement. This conclusion is supported by many previous studies too. The root cause of this reduction of strength is increasing number of atoms in grain boundary region. This creates high energy zones near grain boundary. As a result the initiation of plastic flow begins in the grain boundary. Figure 3.12 (b) shows variation in modulus of resilience of the nanowire with different grain sizes. This plot shows that ability to store elastic energy increases as the grain size increases up to 14.91 nm and after then decreases.

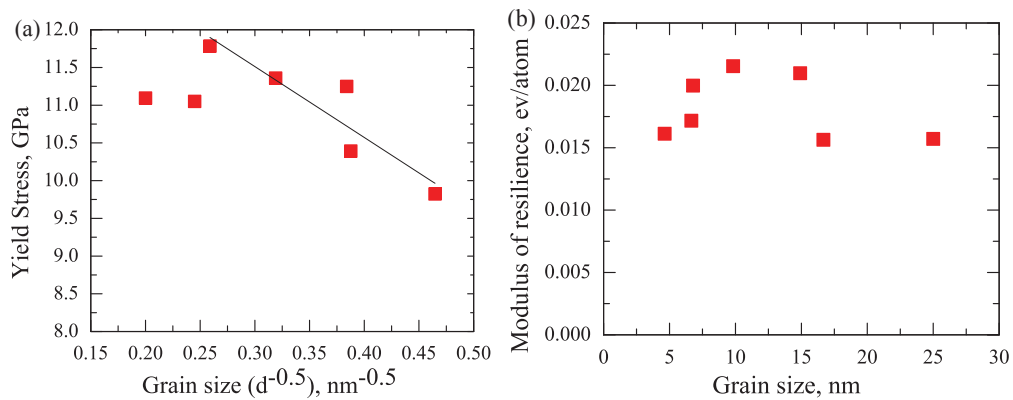


FIGURE 3.12: (a) Variation of yield stress, and (b) modulus of resilience for different grain sizes at 10 K temperature and for 5 nm diameter nanowire.

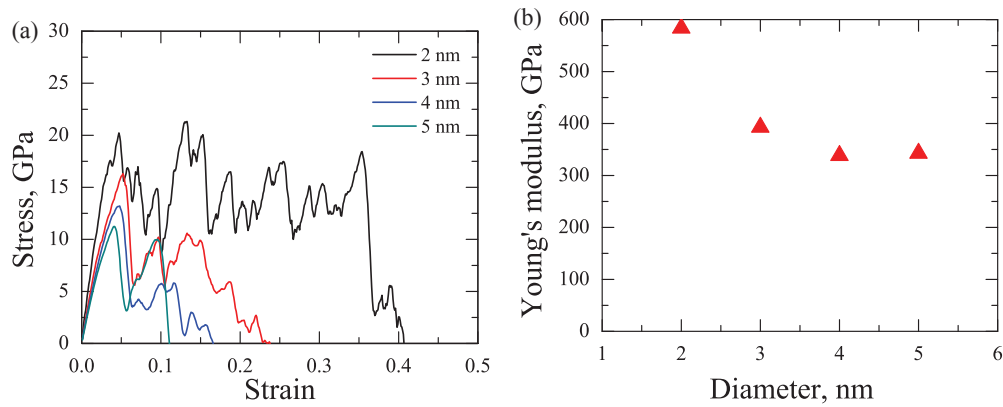


FIGURE 3.13: (a) Stress vs strain plot, and (b) Variation of Young's modulus with diameter of nanowires at 10 K and 6.79 nm average grain size.

### 3.3.2 Impact of Diameter

In order to explore the external size effect on elastic properties of polycrystalline *W* nanowire, diameter of a nanowire with average grain size of 6.79 nm is varied at a temperature of 10 K keeping the length to diameter ratio constant and mechanical responses are observed. The nature of stress vs strain response varies as the size of nanowire is increased from 2 nm to 5 nm. For the smallest nanowire, the stress shows a linear portion at the beginning and then continuous plastic deformation until failure. For 2 nm nanowire no double peak is seen. Similar trend is observed for nanowires with 3 and 4 nm diameters (see, Figure 3.13 (a)). However, for 5 nm diameter, strain hardening and double peaks can be observed. Actually for small sized nanowires, defects are generated and propagated within a small dimension and thus do not get the chance to interact with the grain boundaries before failure. However, in the large size nanowires, there is enough chance of deformation twin to encounter a grain boundary. Moreover, larger nanowires have smaller Young's modulus (see Figure 3.13 (b)). This supports the fact that smaller nanowires have higher strength. Figure 3.14 (a) portrays similar outcome in terms of yield strength of nanowire. Modulus of resilience, however, shows a dip for nanowire with 3 nm diameter. After that increasing the size of the nanowire shows increase in modulus of resilience. This result can be construed from Figure 3.14 (b).

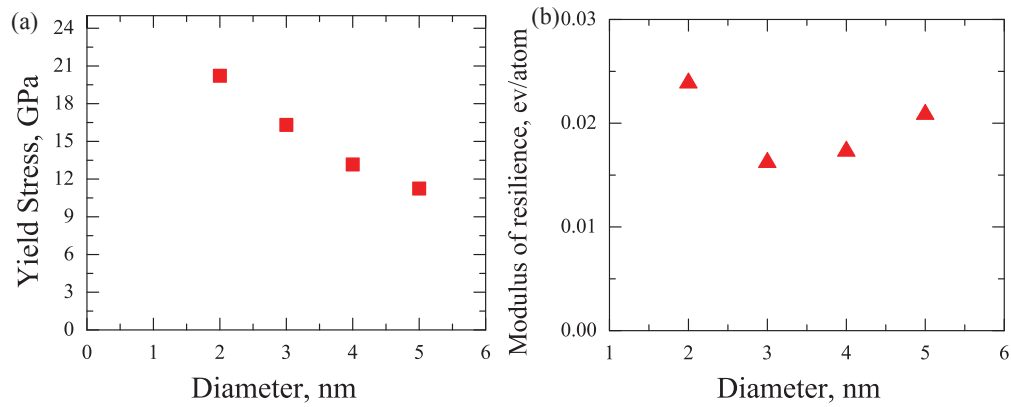


FIGURE 3.14: (a) Variation of yield stress, and (b) modulus of resilience with diameter of nanowires at 10 K and 6.79 nm average grain size.

### 3.3.3 Impact of Temperature

Temperature has a profound impact on the strength of single crystal *W* nanowires. Elevated temperature expedites the failure of nanowire. In order to explore effect of temperature on the elastic properties of polycrystalline *W* nanowire uniaxial tensile tests are performed on a nanowire with 5 nm diameter and 6.79 nm average grain size. Figure 3.15 (a) exhibits that with temperature there is no significant change in the deformation mechanism in the nanowire. However, there is a marked decrease in the strength of nanowire with higher temperature. Figure 3.15 (b) reveals that elevated temperature has an adverse effect on the Young's modulus too. At an elevated temperature, the atoms of nanowire have higher entropy. The amplitude of vibration about the equilibrium position also increases with temperature. This fact contributes to the weakening of nanowire at an elevated temperature. More evidence of this substantiates in the Figure 3.16 (a) where the yield stress of the nanowire is seen to reduce with elevated temperature. Figure 3.16 (b) shows modulus of resilience has an upward trend with temperature. This occurs because of increased ductility in the nanowire with higher temperature.

### 3.3.4 Failure Mechanism

An extensive study on the failure mechanism of different nanowires is undertaken in this work. Since no significant difference in failure mechanism is found for varied temperature, within the range of temperature considered, focus of this section is mainly



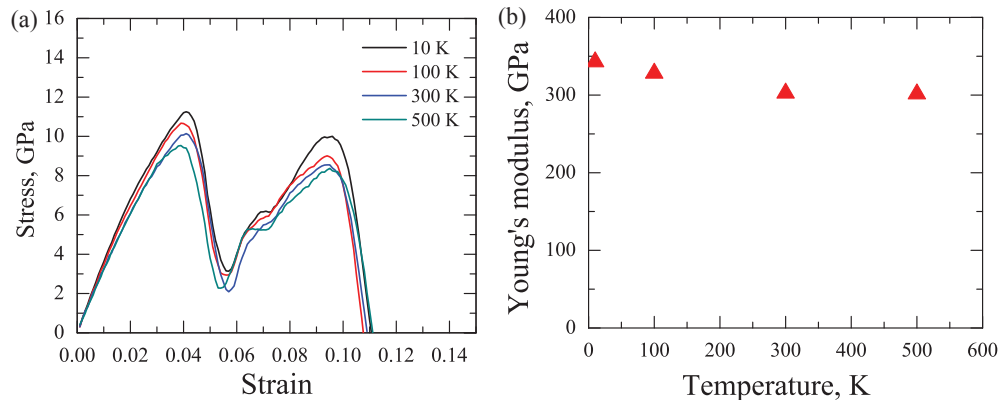


FIGURE 3.15: (a) Stress vs strain plot, and (b) Variation of Young's modulus with temperatures for nanowire of 5 nm diameter and 6.79 nm grain size.

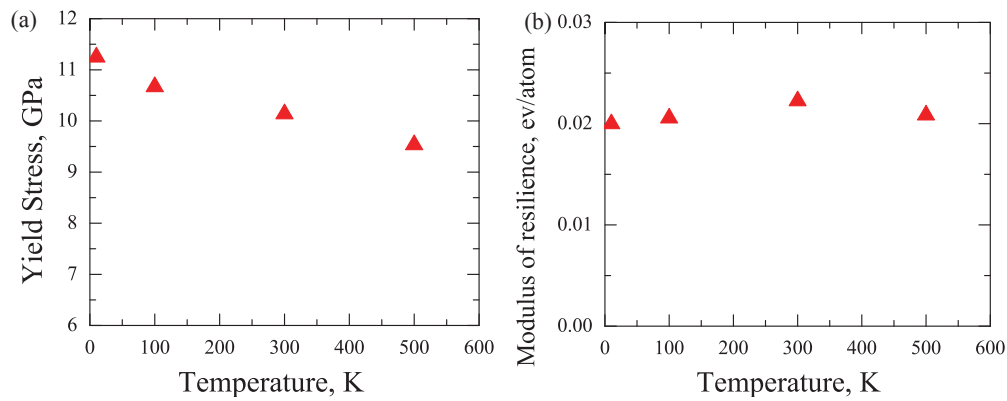


FIGURE 3.16: (a) Variation of yield stress, and (b) modulus of resilience with temperature for nanowire of 5 nm diameter and 6.79 nm average grain size.

to explore roles of diameter and grain size in plasticity of nanowire from atomistic viewpoint. An interesting result has been observed in Figure 3.13 where it can be seen that nanowires with 2, 3, and 4 nm diameter have common pattern in plasticity while nanowire with 5 nm diameter deforms differently. In subsequent part of this paper, fracture of nanowire with 5 nm diameter is extensively studied for different grain sizes. Therefore, atomistic phenomena of failure of nanowire with 2 nm diameter is analyzed in this section as representative case. Figure 3.17 portrays different stages of failure of nanowire with 2 nm diameter and an average grain size of 6.79 nm at 10 K. As can be seen from the figure, at about 7% strain a deformation twin is generated inside the grain from the grain boundary. As the strain increases, the twin travels across the grain and initiates crack in the nanowire. Finally the crack grows and initiates failure. In this case the whole process is twinning-dominant. Presence of dislocation twin during plastic deformation of bcc *W* nanowire is established fact from previous simulations and

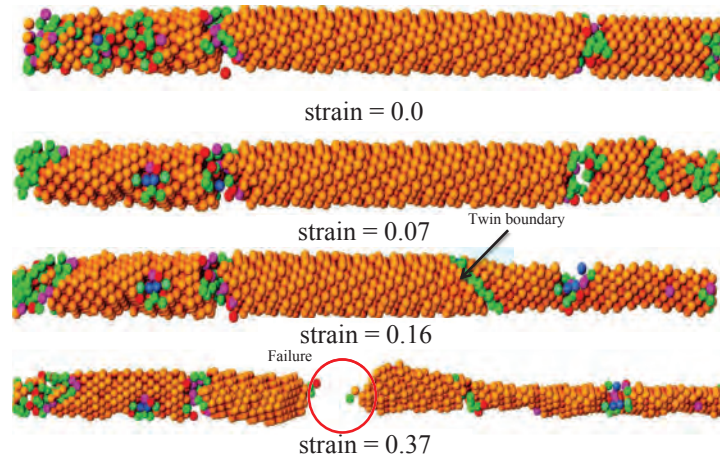


FIGURE 3.17: Atomistic configurations of nanowire of 2 nm diameter and 6.79 nm average grain size at 10 K at different stages of uniaxial tensile test.

experiments [13, 49]. Growth of  $\frac{1}{6} \langle 111 \rangle$  partial dislocation on adjacent  $[211]$  planes gives rise to twin boundary in single crystal bcc nanowires [13] at high strain rates. In this work similar twin growth and glide is observed during plasticity. This twinning is responsible for the ductility of *W* nanowire. Gliding of twin boundary originates from consecutive slide of  $\frac{1}{6} \langle 111 \rangle$  partial dislocations on  $[211]$  planes.

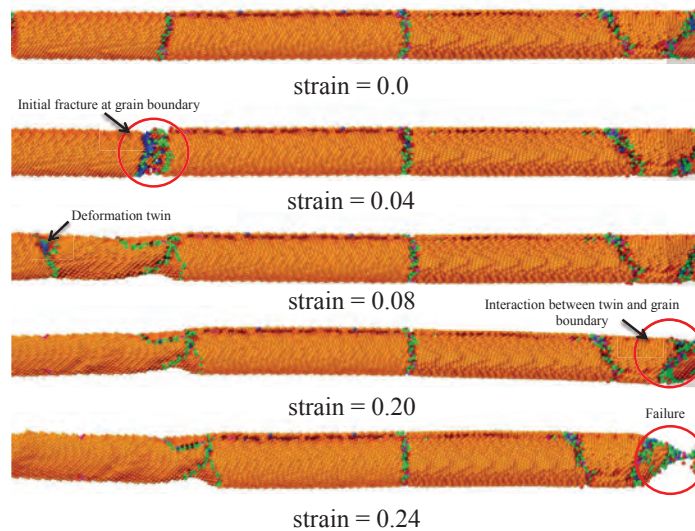


FIGURE 3.18: Atomistic configurations of nanowire of 5 nm diameter and 14.91 nm average grain size at 10 K at different stages of uniaxial tensile test.

However, a different phenomenon is observed when fracture of nanowire of different grain sizes are studied. Depending on the size of the grain the failure mechanism can be

either grain boundary sliding or twinning-dominated. To observe impact of grain size on the fracture mechanism, a nanowire of 5 nm diameter and average grain sizes of 14.91, 6.79 and 4.63 nm are analyzed at 10 K temperature. For nanowire with 14.91 nm grain size, initial fracture is seen to be emanating from the triple junction of grain boundaries at 4% strain. From the triple junction deformation twin propagates through the grain. At about 20% strain the twin seems to interact with the grain boundary of nanowire. This impedes the motion of deformation twin and gives rise to the second peak in the stress vs strain curve (refer to Figure 3.11(a)). Ultimate failure occurs where the twin interacts with the grain boundary.

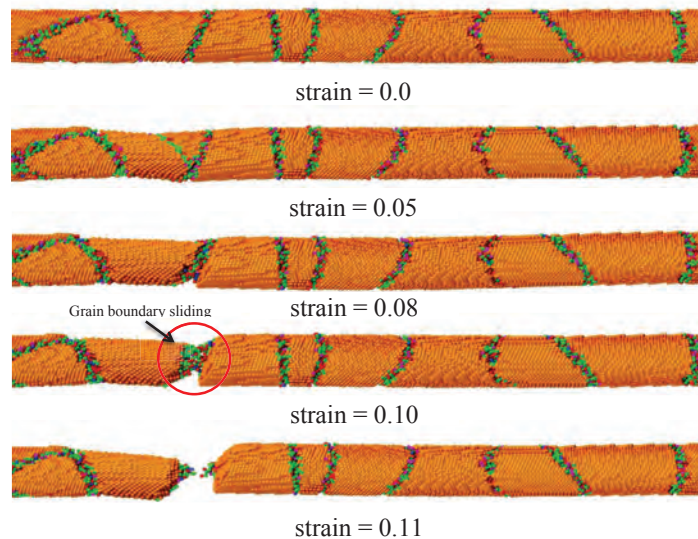


FIGURE 3.19: Atomistic configurations of nanowire of 5 nm diameter and 6.79 nm average grain size at 10 K at different stages of uniaxial tensile test.

Now if the average grain size is reduced further, as shown in Figure 3.19, where the average grain size is considered 6.79 nm, the fracture mechanism transforms to grain boundary sliding. Figure 3.19 reveals that for 6.79 nm average grain size, the grain boundary sliding begins at 10% strain. The most vulnerable part of the nanowire is the triple junction where atoms have higher energy. The sliding begins from this triple junction. Later, within a very small strain range complete rupture occurs.

Interestingly, for this particular case, twin peak is also observed. This is due to some intragranular dislocation activities. DXA analysis shows presence of  $\frac{1}{2} \langle 111 \rangle$  dislocation inside the grains of nanowire due to high stress. However, this dislocation does not produce ultimate failure of the nanowire. Presence of this dislocation causes

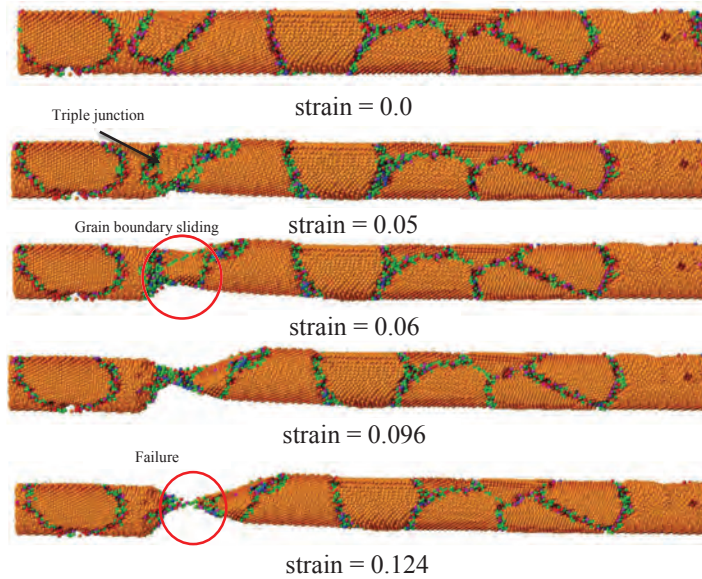


FIGURE 3.20: Atomistic configurations of nanowire of 5 nm diameter and 4.63 nm average grain size at 10 K at different stages of uniaxial tensile test.

strain hardening which creates a rise in stress (refer to Figure 3.11(a)). Ultimately grain boundary sliding appears to be the governing mechanism of failure. For finer grain (see Figure 3.20) with average grain size of 4.63 nm, grain boundary sliding begins from a triple junction at about 6% strain and continues until failure occurs at 12.4% strain. No significant intragranular dislocation activity is observed for this grain size.

### **3.4 Summary**

In this chapter, through atomistic simulation, deformation mechanism in both single and polycrystalline Tungsten nanowires has been explored. It is found that deformation twinning is the major mode of deformation in case of single crystal nanowire. However, the mode of deformation in polycrystalline nanowires is highly dependent on the grain boundaries. Additionally, it is observed that external diameter, temperature, and loading orientation serve as key factors governing deformation in nanowires.

# Chapter 4

## Creep Behavior of $W$ at Nanoscale

### 4.1 Introduction

In this chapter, impact of grain size, temperature, and applied stress on the creep mechanism of nanocrystalline tungsten is analyzed using molecular dynamics technique. A cubic sample of tungsten nanocrystal is considered and the applied constant stress ranges from 2.5 to 5.5 GPa. For analysis, temperature is varied from 1600 K - 2200 K while grain sizes considered are 2.38 nm, 2.86 nm, 3.57 nm, and 4.76 nm. Since attaining actual creep rate in atomistic simulation is beyond the scope of computational facilities used for this work, high values for applied stress and temperature are considered to simulate creep mechanism within nanoseconds duration. Before applying external stress, the structure is minimized using conjugate gradient method with time step of 0.001 ps. Then the structure is equilibrated at a certain temperature using *NPT* ensemble for 200 ps. Finally, a constant tensile stress is applied along x-direction while keeping other directions stress-free for another 200 ps.

#### 4.1.1 Nature of Creep Curves

In order to observe the impact of temperature and applied stress the nanocrystalline tungsten sample with grain sizes of 4.76 nm, 3.57 nm, 2.86 nm, and 2.38 nm are subjected to different levels of applied stresses from 2.5 GPa to 5.5 GPa at temperatures

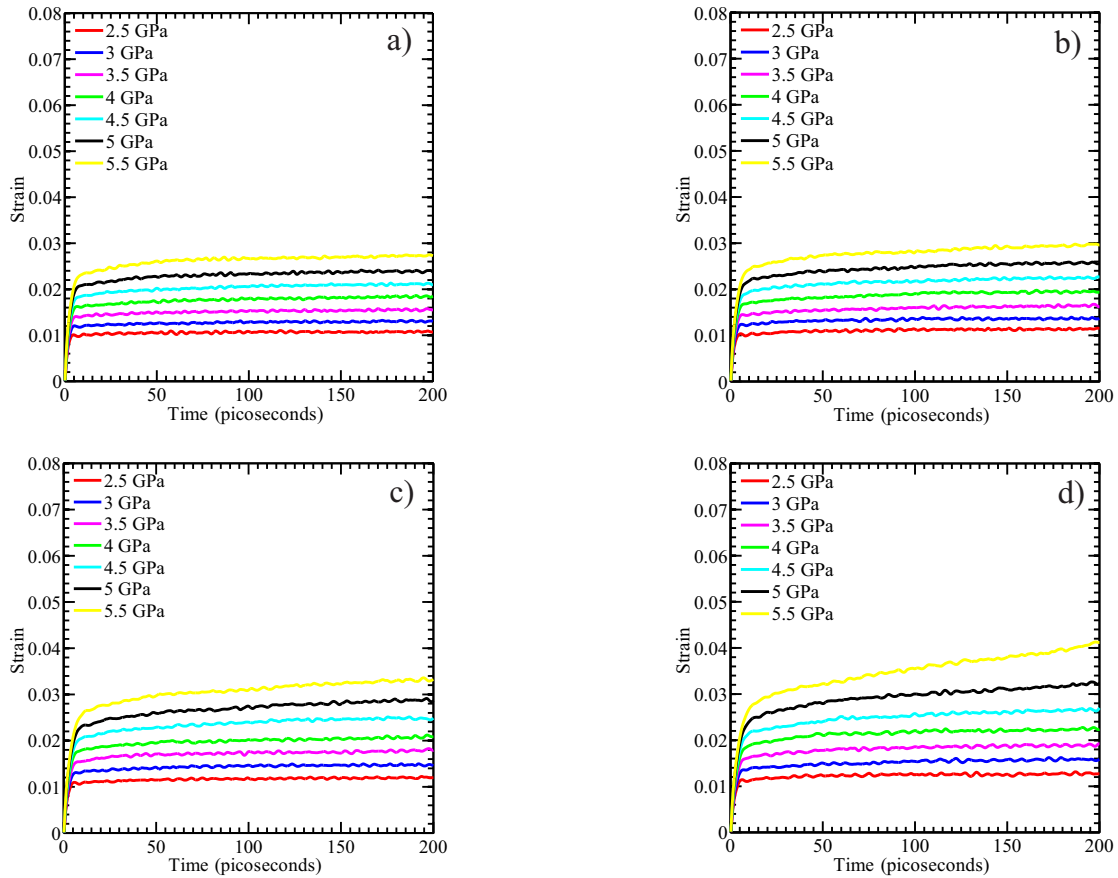


FIGURE 4.1: Creep curves for different applied stresses at a) 1600 K, b) 1800 K, c) 2000 K, and d) 2200 K for grain size of 4.76 nm.

ranging from 1600 K to 2200 K. Resulting creep curves are shown in Figures. 4.1, 4.2, 4.3, and 4.4. From Figure 4.1 it can be seen that for every instance of applied stress, initially there is a spike in the strain. This sudden rise of strain is known as the primary stage of creep. However, the focus of this study is more on the secondary stage or steady-state creep which is seen just after the initial strain spike. In this stage the strain rate is more or less constant over a long period of time. It is evident from the Figure 4.1 that with higher applied stress predictably the strain is higher. There is marked increase in the SSCR as the temperature is varied from 1600 K to 2200 K. Similar pattern was also observed in previous works [61, 67]. For grain size of 4.76 nm, there is no observable tertiary creep zone within 200 ns. Creep curves for grain size of 3.57 nm are shown Figure 4.2. This is finer grain size and in contrast to grain size of 4.76 nm one can see significant tertiary creep for 5.5 GPa applied stress under 2000 K and 2200 K temperature. Two cases have common features of elevation of strain with applied load

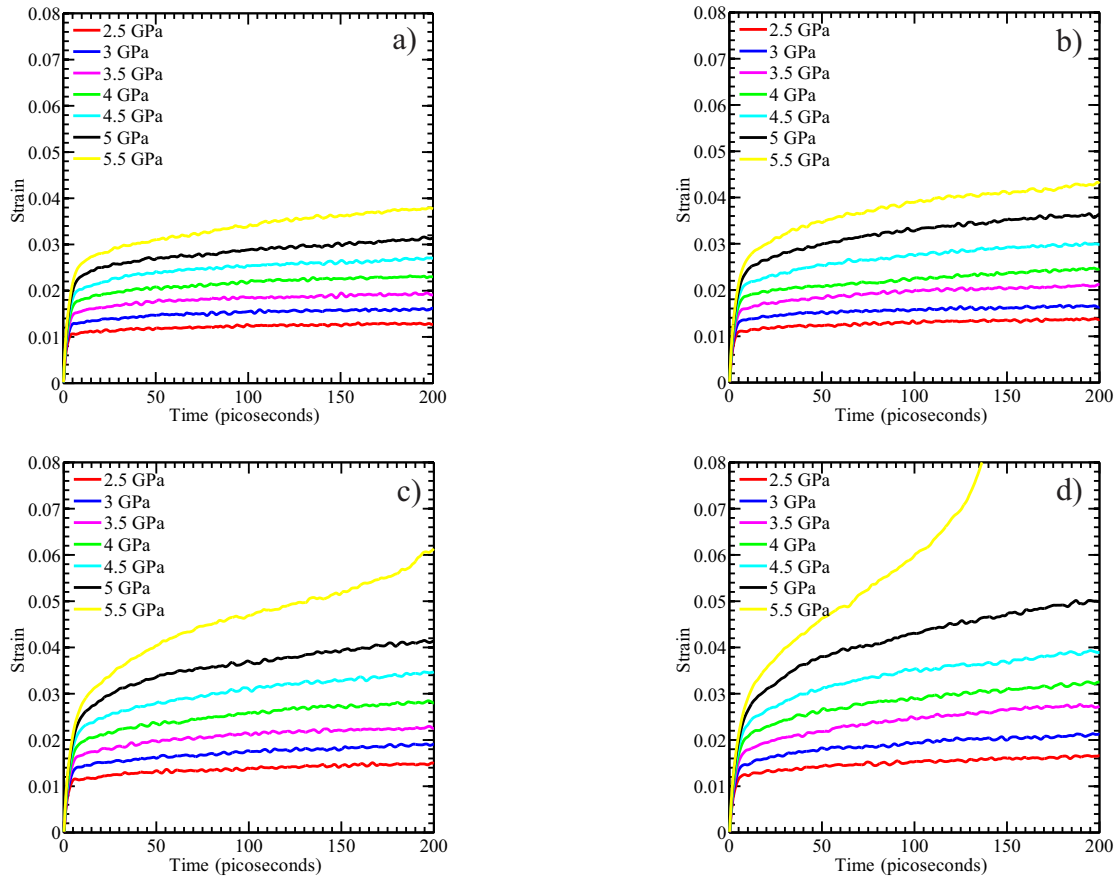


FIGURE 4.2: Creep curves for different applied stresses at a) 1600 K, b) 1800 K, c) 2000 K, and d) 2200 K for grain size of 3.57 nm.

and higher creep rate with elevated temperature. With finer grain size, strain seems to increase for same applied stress and temperature. This indicates that finer grain size is actually helping increase the creep. This is exactly opposite nature of bulk materials which tend to show higher creep resistance as grain is refined. Observation of Figures 4.3 and 4.4 further confirms the aforementioned trends so much so that for grain size of 2.38 nm, significant tertiary creep is observed to start from very early stages and from stress as low as 4 GPa. Hence, steady-state creep stage is quite small for this case.

To test the effect of presence of grains on creep deformation, single crystal tungsten-cube of same dimensions as the nanocrystalline samples is exposed to an applied stress of 5 GPa at 1800 K temperature. The resulting creep curve is compared with that of nanocrystalline samples in Figure 4.5. It is observed that for single crystal tungsten, after the initial spike, the strain does not increase rather reaches an almost constant value. This means there is no observable steady-state creep deformation. On the other



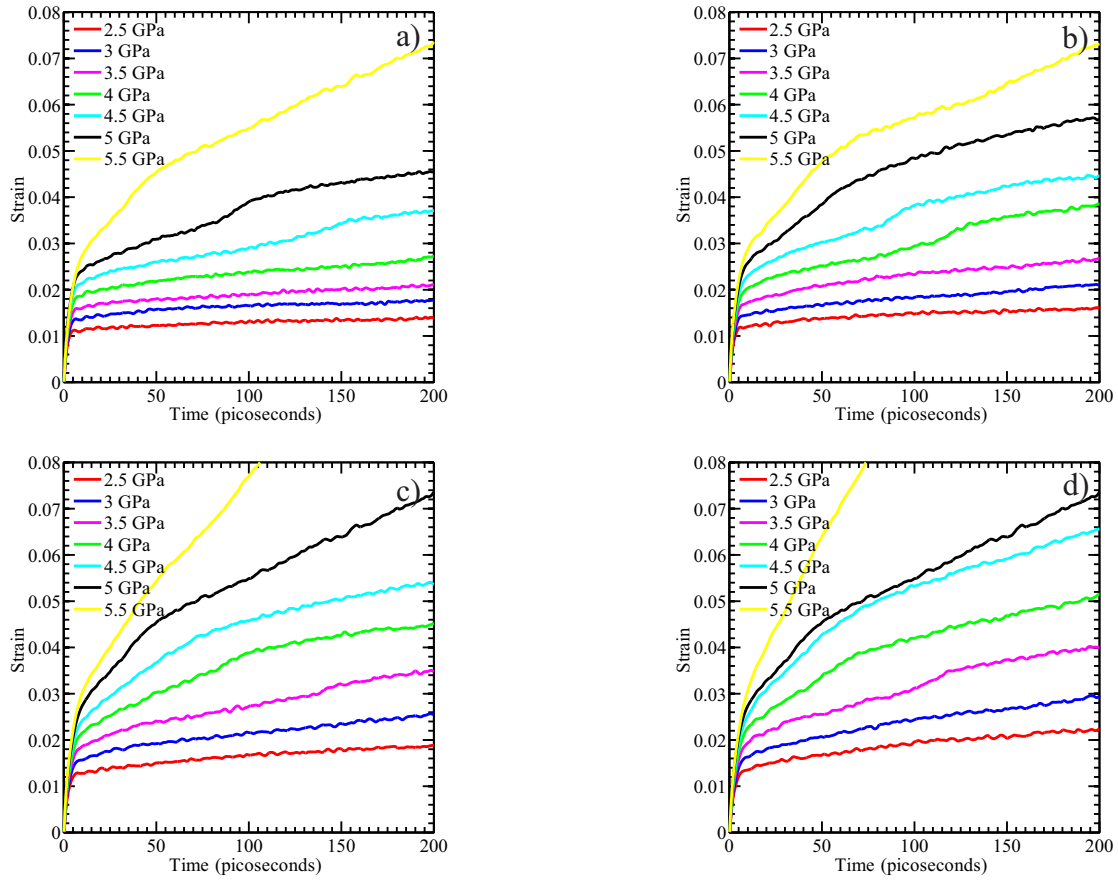


FIGURE 4.3: Creep curves for different applied stresses at a) 1600 K, b) 1800 K, c) 2000 K, and d) 2200 K for grain size of 2.86 nm.

hand, for polycrystalline samples with grain sizes of 2.38 nm to 4.76 nm clear signs of creep deformation are manifested. It is also observed from Figure 4.5 that for the nanograined samples, the primary creep strain is smaller but the steady-state rate of strain is much higher compared to the single crystal sample. It has to be kept in mind that the grain sizes considered in this study falls within the inverse Hall-Petch regime for  $W$  as mentioned in chapter 4. If the size of the grain is increased, the primary creep may become higher than that of single crystal  $W$  sample.

Wang et al. [68] observed similar creep transition in his work for Copper nanocrystal. Their results on impact of stress on the creep rate of Cu nanocrystal with grain size of 10.7 nm at 960 K temperature are shown in Figure 4.6. It is seen that as the applied stress is raised, the creep rate is increasing. Moreover, the magnitude of stress is quite comparable to this work within 200 ps.

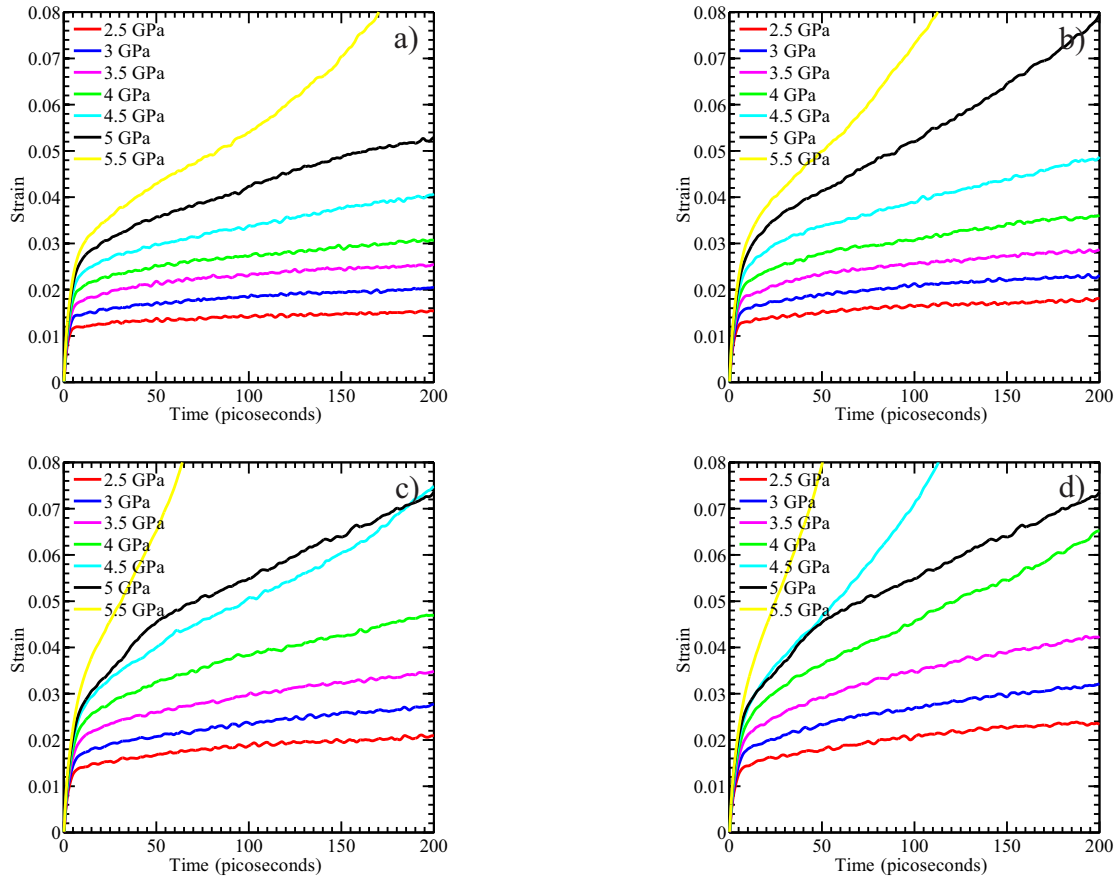


FIGURE 4.4: Creep curves for different applied stresses at a) 1600 K, b) 1800 K, c) 2000 K, and d) 2200 K for grain size of 2.38 nm.

### 4.1.2 Impact of Grain Size

Influence of varying grain size on the creep rate and creep mechanism can be observed from Figure 4.7. According to Eqn. 1.4 there must be a power-law relationship between the creep rate and inverse of grain size for constant temperature and stress level. The exponent,  $p$ , aptly known as the grain size exponent, suggests the creep mechanism. It can be evaluated from the slope of the curves shown in Figure 4.7 and the values are listed in Table 4.1. Refining the grain size of the cubic sample seems to increase the propensity to suffer creep deformation. Values of the grain size exponents give an idea about the underlying physical process. For example value of  $p = 2$  suggests that the governing creep mechanism is Nabarro-Herring creep or lattice diffusion creep. Similarly,  $p = 3$  is suggestive of grain boundary diffusion creep while  $p > 3$  indicates initiation of dislocation dominated creep mechanism. The range  $2 < p < 3$  suggests that the creep mechanism is

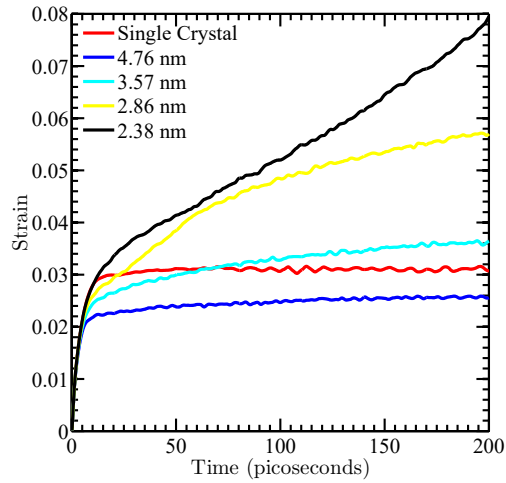


FIGURE 4.5: Comparison of creep curves between single-crystal and nanocrystalline tungsten at 1800 K under 5 GPa stress.

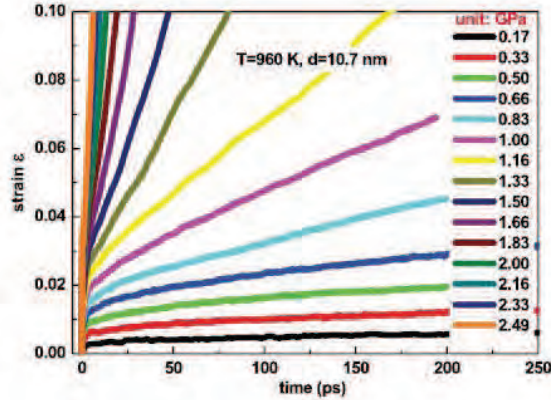


FIGURE 4.6: Creep curve calculated for Copper by Wang et al.

a confluence of lattice diffusion, grain boundary diffusion, and grain boundary sliding creep [61]. This is a direct result of high volume of grain boundary in the nanocrystalline sample considered. The grain boundaries act as source and sink for dislocation. Moreover, along the grain boundaries, diffusion is fast for nanocrystals. As the applied stress is raised, value of  $p$  increases to more than 4 suggesting dislocation-dominated creep. Grain boundary sliding also plays a part in accommodating the grains at higher applied stress. Table 4.1 exhibits that the grain size exponent gradually shifts from a value of 2-3 to values above 4 as the value of applied stress is raised. In bulk materials, power-law creep does not exhibit a grain size dependence. This happens because in bulk materials dislocation activities are confined to inside of the grain and there is little interaction with grain boundaries. On the other hand, in fine grain nanocrystalline

material, the grains being small, there is frequent interaction of grain boundary and dislocation. As a result, grain size largely influences the creep phenomenon. Figure 4.7 presents a graphical picture of the impact of changing stress and grain size on the SSCR at different temperatures. The general result is increment of SSCR with smaller grain size and higher applied stress. Moreover, higher temperature seems to aid the SSCR irrespective of grain size and applied stress. Impact of  $p$  is explained further with help of atomistic configurations in §4.1.5.

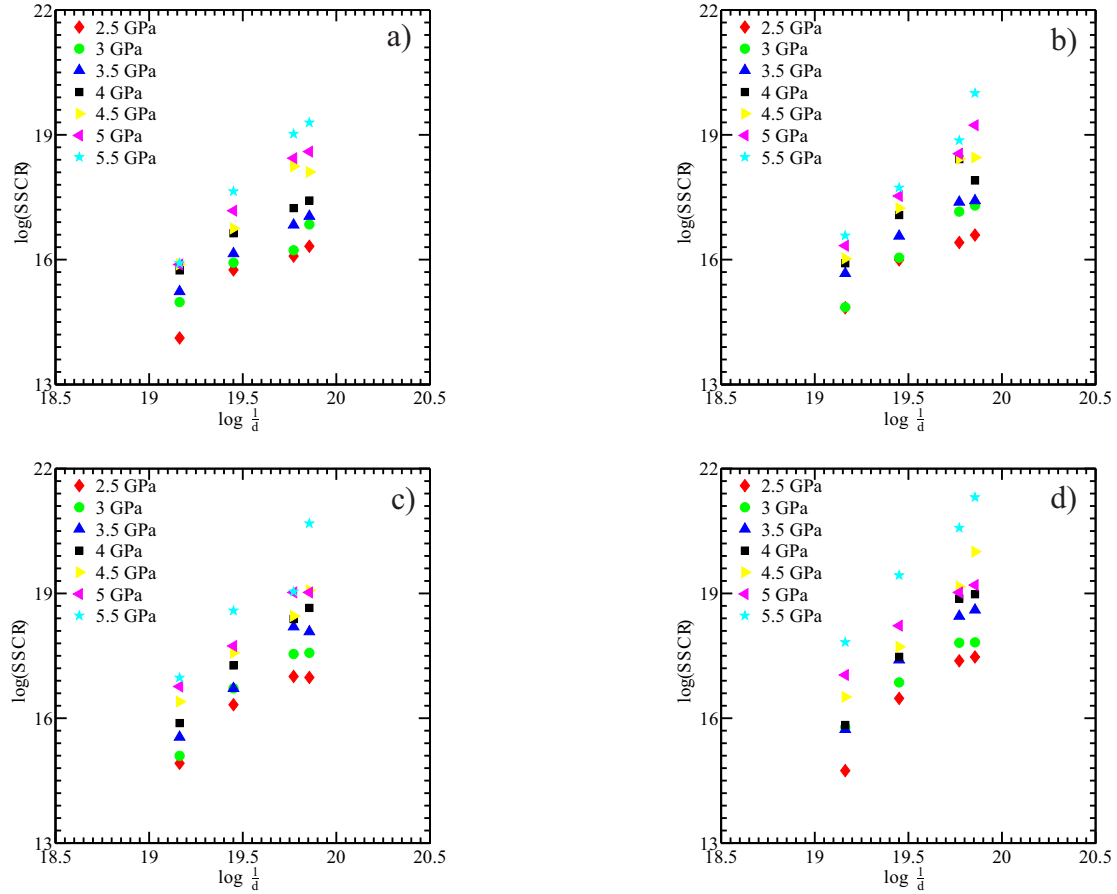


FIGURE 4.7: Variation of steady-state creep rate with inverse grain size for applied stress at a) 1600 K, b) 1800 K, c) 2000 K, and d) 2200 K.

### 4.1.3 Impact of Stress

Applied stress is another dictating factor for the nature of creep mechanism in nanocrystalline  $W$ . In creep curves (Figures 4.1, 4.2, 4.3, and 4.4) it is seen that for a particular

Temperature (K)	Stress, (GPa)						
	2.5	3	3.5	4	4.5	5	5.5
1600	2.94	2.35	2.55	2.36	3.50	3.98	4.86
1800	2.39	3.57	2.59	3.28	3.61	3.95	4.53
2000	2.97	3.54	3.91	3.96	3.63	3.44	4.49
2200	3.89	3.02	4.11	4.61	4.84	3.08	4.75

TABLE 4.1: Grain size exponents ( $p$ ) for different temperatures and stresses.

grain size creep strain increases with the applied stress level, irrespective of the temperature. From the creep curves, the SSCR for different applied stresses and grain sizes are extracted which are then plotted in log-scale for 1600 K, 1800 K, 2000 K, and 2200 K temperatures in Figure 4.8. From the figure, it is evident that applied stress has a positive impact on the creep rate. Higher stresses aid both vacancy diffusion and dislocation nucleation in material which in turn accelerate the creep deformation. Moreover, grain boundaries act as fast diffusion path for vacancies that pave the way for higher creep rate under the applied stress.

Temperature (K)	Grain size, (nm)			
	4.76	3.57	2.86	2.38
1600	2.24	2.34	3.94	3.60
1800	2.34	2.41	3.12	4.05
2000	2.80	2.58	2.59	4.04
2200	3.36	3.17	3.43	4.22

TABLE 4.2: Stress exponents ( $n$ ) for different temperatures and grain sizes.

From the linear relationship of Figure 4.8, one can determine the stress exponent,  $n$ , of Eqn. 1.4. Values of  $n$  is suggestive of the creep mechanism prevailing in nanocrystalline  $W$ . Table 4.2 lists the values of  $n$  for temperature and grain sizes considered in the work and shows that grain refinement and temperature both raise the values of  $n$  in general. For the cases where  $2 < n < 3$ , the creep mechanism is supposed to be grain boundary and lattice diffusion concomitantly. When  $n$  reaches a value of 3 or higher, the creep mechanism can be referred to as dislocation creep. In general, the value of  $n$  increases with reducing grain size. However, in Table 4.2, two exceptions are observed (for 2000 K, 4.76 nm grain size and for 2200 K, 4.76 nm grain size), where values of  $n$  are actually decreasing at the next grain refinement stage. This trivial difference might be due to nature of diffusions originally present in the atomic structure.

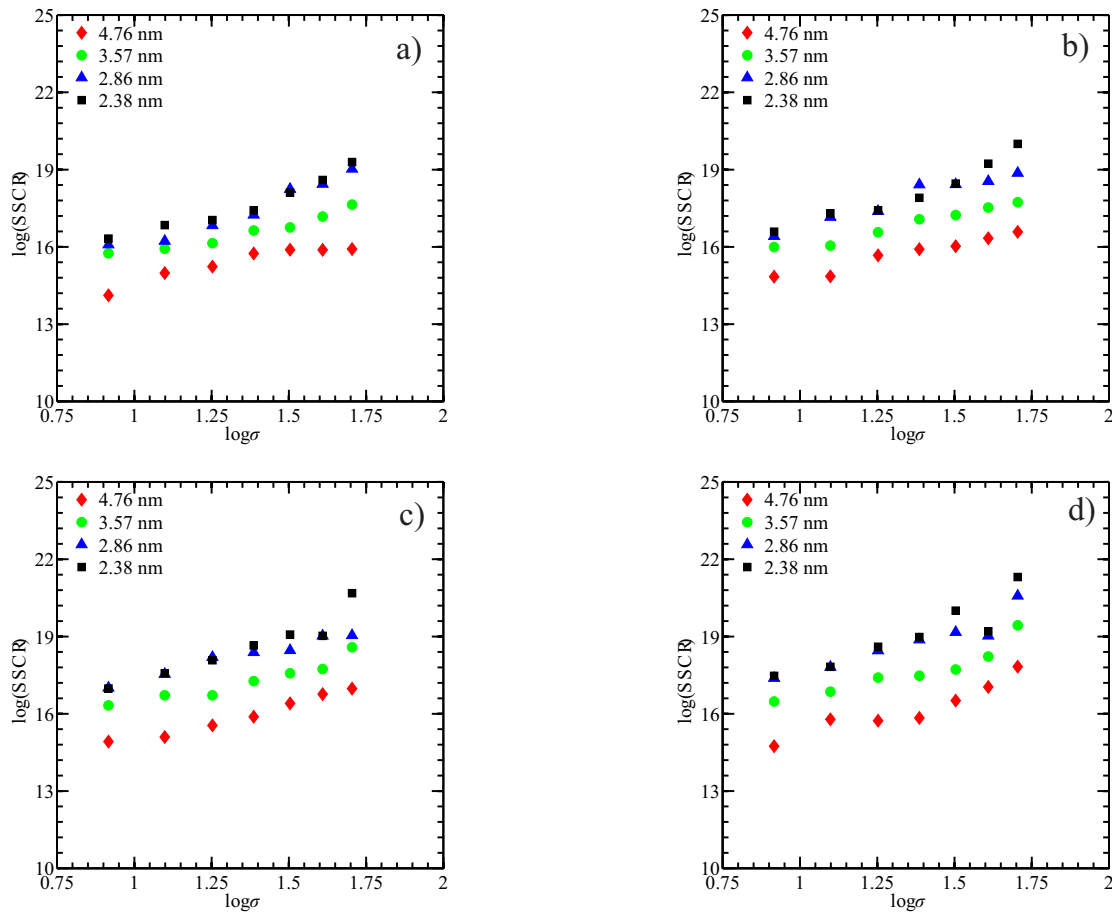


FIGURE 4.8: Variation of steady-state creep rate with applied stress for different grain sizes at a) 1600 K, b) 1800 K, c) 2000 K, and d) 2200 K

#### 4.1.4 Impact of Temperature

Figure 4.9 reveals the impact of temperature on the SSCR as a function of applied stress and grain size. Previous discussions already explored the impact of higher temperature on creep rate. High temperature is conducive for creep deformation which is evident in Figures 4.1 to 4.4 as well as Figure 4.9. Physical reason behind this is quite straight forward. Higher temperature weakens the atomic structure by creating intense vibrations. Hence, it becomes easier to deform, especially, when an external stress is applied. Moreover, Table 4.1 and 4.2 support the idea that increasing the temperature has impact on the creep mechanism as it is evident that both grain size and stress exponents increase with temperature. This also implies a shifting in the creep mechanism where elevated temperatures promote the diffusion process and dislocation nucleation in the

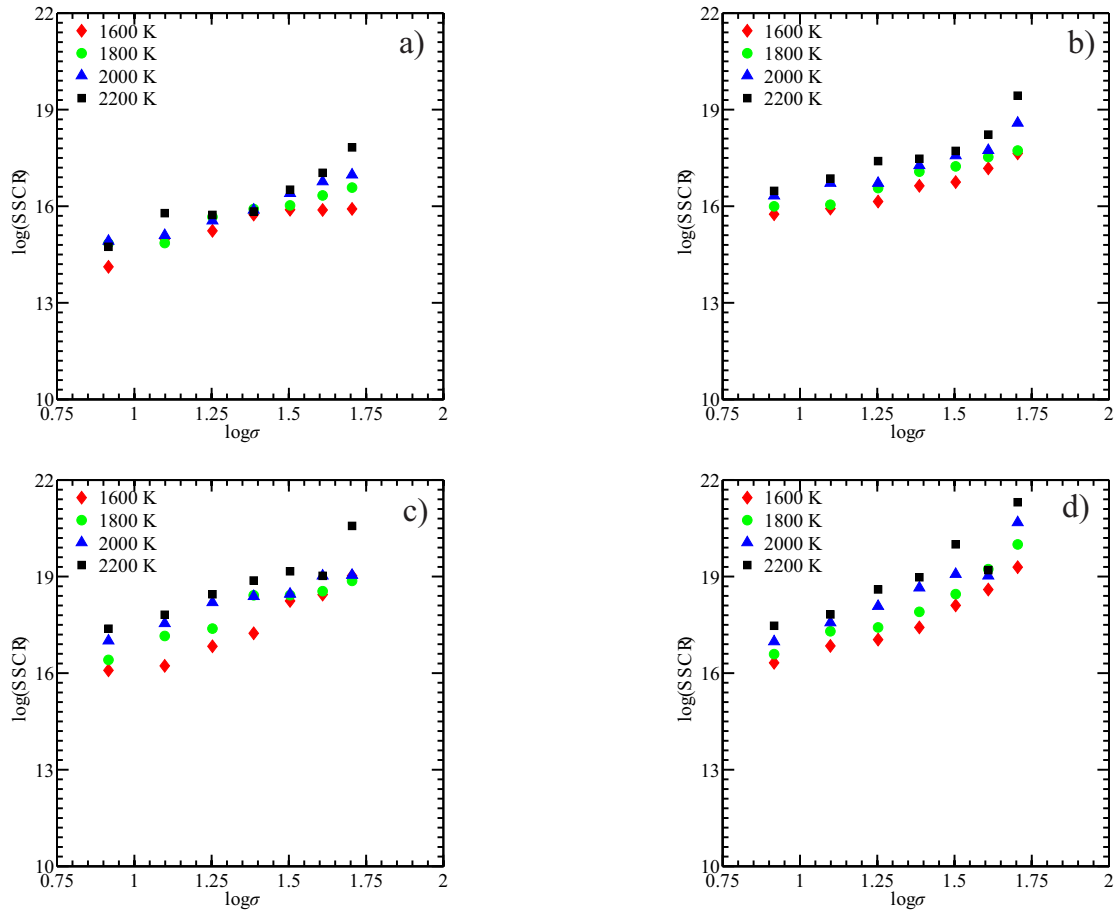


FIGURE 4.9: Variation of steady-state creep rate with applied stress at grain sizes of a) 4.76 nm, b) 3.57 nm, c) 2.86 nm, and d) 2.38 nm

structures. Elevated temperature aids the diffusion and dislocation nucleation resulting in higher probability of creep.

#### 4.1.5 Creep Mechanism

In order to test the veracity of our argument on transition of creep mechanism from diffusion to dislocation, diffusion coefficients are calculated for different temperatures and grain sizes for a fixed stress level of 3.5 GPa. At first, the MSD is calculated for different cases (refer to Figure 4.10) as function of time and from the slope of these plots, diffusion coefficient,  $D$ , is calculated using Einstein's relation [60],

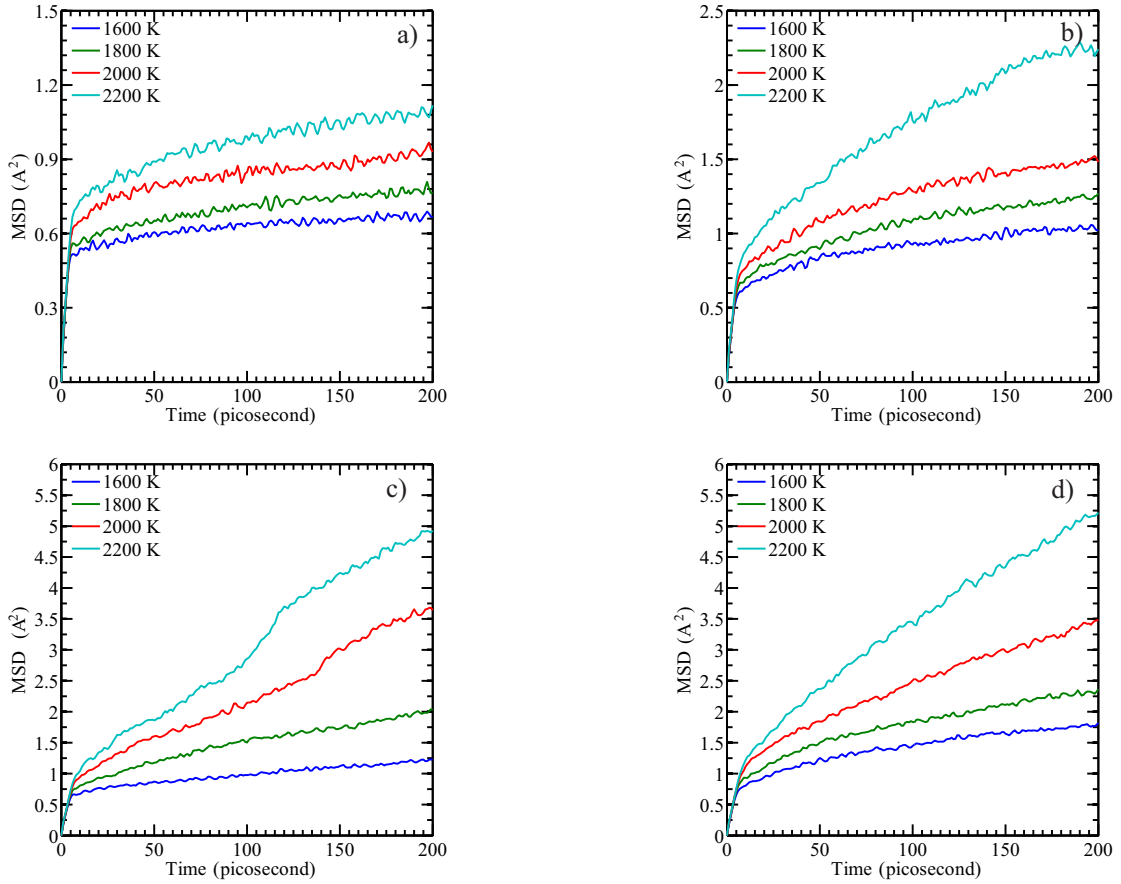


FIGURE 4.10: Mean square displacements of the  $W$  atoms for a) 4.76 nm, b) 3.57 nm , c) 2.86 nm, and d) 2.38 nm average grain size under 3.5 GPa stress.

$$D = \frac{1}{6t} \langle (r_i(t) - r_i(0))^2 \rangle. \quad (4.1)$$

The diffusion coefficients are then plotted in Figure 4.11 on an Arrhenius plot. From Figure 4.10, one can see that, similar to the creep curves, there is an initial spike in the MSD values for primary creep. After the initial surge in MSD, the deformation occurs at a constant rate over the subsequent deformation period. Higher temperature lowers the activation energy which makes the diffusion of atoms easier. It manifests itself in Figure 4.10 as one can see greater deformation as temperature is raised. The Arrhenius plot of Figure 4.11 shows the dependency of diffusion coefficient on temperature. This relationship can be expressed as [60],

$$D = D_0 \exp \frac{-\Delta G}{k_B T} \quad (4.2)$$



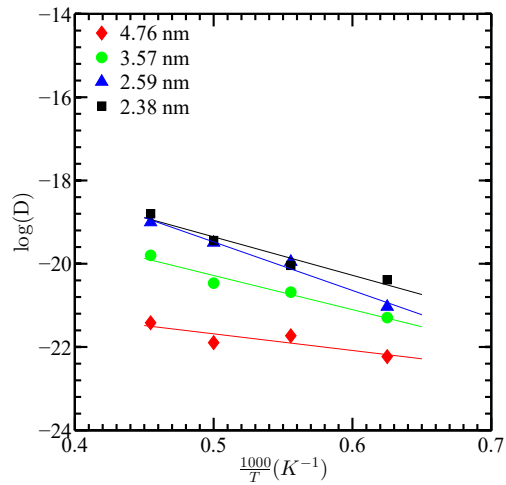


FIGURE 4.11: Diffusion coefficient as a function of temperature and grain size under 3.5 GPa applied stress.

where  $D_0$  is the diffusion pre-exponential factor and  $\Delta G$  is the activation energy for diffusion. The diffusion coefficient shows a positive relationship with temperature.  $D_0$  also depends on grain size, which has been calculated by fitting the lines in Figure 4.11 and it is found that the value increases from  $2.81 \times 10^{-9} A^2/ps$  to  $3.97 \times 10^{-7} A^2/ps$  if the grain size is reduced from 4.76 nm to 2.38 nm. It proves the propensity for diffusion as the grain is refined in a nanocrystal. Hence, the hypothesis of diffusion as the key mechanism of creep deformation in nanocrystalline *W* is supported by the simulation results.

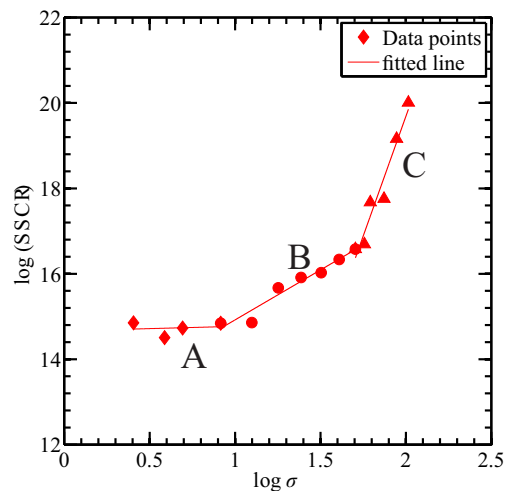


FIGURE 4.12: Change in stress exponent for gradually increasing stresses for grain size of 4.76 nm at 1800 K.

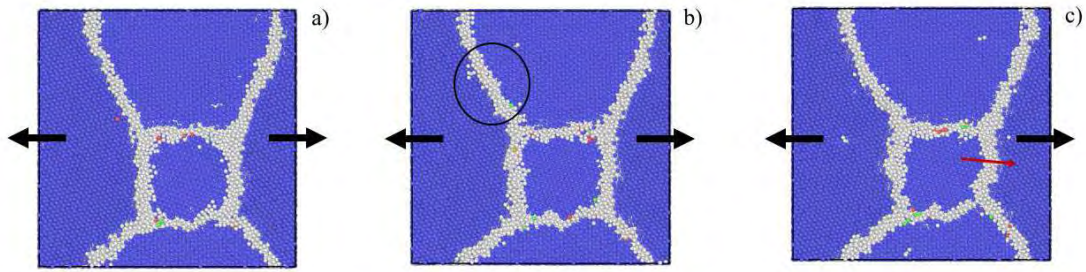


FIGURE 4.13: Atomistic configurations of  $W$  with grain size of 3.57 nm at 1800 K under 3 GPa stress. a) at  $t = 0$  ps, b) at  $t = 100$  ps, and c) at  $t = 200$  ps.

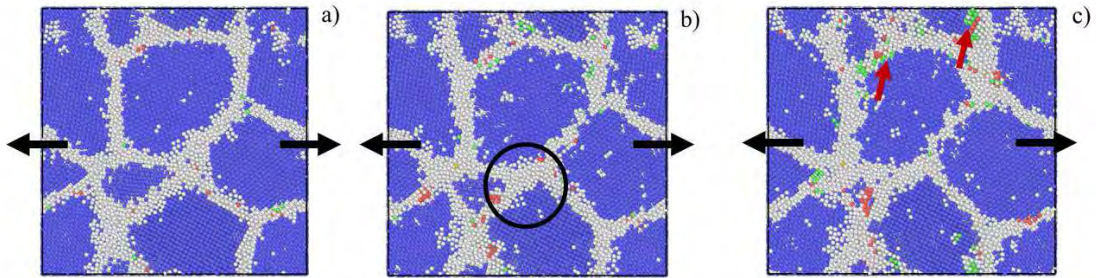


FIGURE 4.14: Atomistic configurations of  $W$  with grain size of 2.86 nm at 2200 K under 4 GPa stress. a) at  $t = 0$  ps, b) at  $t = 100$  ps, and c) at  $t = 200$  ps.

It is already established that by applying higher stress, the creep mechanism can be changed from vacancy and grain boundary diffusion to grain boundary sliding to dislocation-controlled creep. However, application of stress above a threshold value leads to breakdown of power-law creep. For verifying this transition of stress a sample with grain size 4.76 nm is applied with a range of stress from 1.5 to 7.5 GPa at 1800 K temperature. Resulting logarithm of SSCR-logarithm of stress plot is drawn in Figure 4.12. There are three distinct parts of this plot. In section A of the plot, the stress exponent,  $n$ , is nearly 1 which indicates lattice diffusion dominated creep mechanism. However, as the stress is increased, in section B the  $n$  is 2.34 suggesting a combination of lattice diffusion and grain boundary diffusion creep mechanism. If the stress is further increased, in section C,  $n$  becomes exceptionally high (above 10) indicating a break-down of power-law controlled creep in nanocrystalline  $W$ . This behaviour is also observed experimentally for high values of stresses. With a view to examining the atomic picture of different creep mechanisms, atomic configurations of nanocrystalline  $W$  sample with grain size of 3.57 nm at 1800 K temperature and under an applied stress of 3 GPa are presented in Figure 4.13. Three different instances of the creep process are exhibited in the Figure 4.13.

Figure 4.13 a) shows the initial configuration of nanocrystalline  $W$  sample after minimization (at  $t = 0$  ps). It shows clearly defined grain boundaries and minute presence of stacking faults. Figure 4.13 b) presents the picture at  $t = 100$  ps where slight elongation of grain along the direction of applied stress is observed. Moreover, along the grain boundaries, the strain or deformation is observed to be the most prominent. This indicates the presence of grain boundary diffusion in the structure at this time. Finally, Figure 4.13 c) shows the structure at  $t = 200$  ps where more diffusion along the grain boundary is observed. However, the central grain suffers a rotation. This is an evidence of grain boundary sliding and rotation as a supporting mechanism for creep in nanocrystalline  $W$  at nanoscale. These atomic pictures match with the qualitative analyses made in section §4.1.3. Moreover Table 4.1 shows that at 1800 K temperature and 3 GPa stress  $p$  is 3.57. This value is a bit high for purely diffusional creep mechanism. However, presence of grain rotation suggests that this accommodating mechanism might be the reason for this high value. Figure 4.14 shows the atomic configurations of nanocrystalline  $W$  with grain size 2.86 nm at 2200 K temperature and under applied stress of 4 GPa. This particular sample is taken for presentation in order to adumbrate the key changes in deformation mechanism for higher applied stress and smaller grain size. Figure 4.14 a) shows the atomic configuration at  $t = 0$  ps which is the minimized structure of the nanocrystalline sample. A considerable difference is observed in the sample compared to the case of Figure 4.13 a). Relatively more stacking faults are present in this structure. This is obvious since higher temperature is conducive to dislocation nucleation. After 100 ps (see, Figure 4.14 b)) diffusion along the grain boundary is seen to be increased. Moreover, the number of stacking faults also increased. It proves a simultaneous presence of grain boundary diffusion and dislocation mechanism in this stage. Finally, at  $t=200$  ps (refer to Figure 4.14 c)), there is intense diffusion of atoms coupled with more dislocations in the sample. This evinces the fact that under high stress, dislocation nucleation becomes the controlling mechanism of creep while grain boundary diffusion acts as supporting mechanism. Under this stress and temperature, dislocation glide and climb is supposed to be the cardinal failure mechanism. However, due to very small time-scale considered in the work the glide and climb could not be observed. Grain growth is another factor which can not be avoided but given the length and timescale considered, effect of grain growth can be neglected. This result is also supported by the results of grain size exponents mentioned in section 4.1.2. From Table

4.1, one can see that for 2200 K temperature and 4 GPa pressure, value of  $p$  is 4.61 suggesting a dislocation dominated creep deformation. Atomistic pictures actually provide further evidence for that conclusion.

## 4.2 Summary

The chapter extensively discusses the findings of atomistic investigation on the factors governing the creep in nanoscale Tungsten. It is observed that through applied stress one can transform the creep mechanism from diffusion to dislocation dominated. Moreover, higher temperature and refined grain size usually aid the creep rate in materials. One interesting finding is that under high sustained stress the power law can not describe the creep phenomenon in nanocrystalline Tungsten. These key outcomes are extensively discussed with the help of atomistic snapshots.

# Chapter 5

## Conclusions

The entire work involves two different but related studies. Considering the high temperature and high stress applications of  $W$ , it is chosen as the material for study in this work. At first single crystal nanowires are analyzed to find out their deformation behaviors. Later, polycrystalline nanowires are considered to find out the relationship between the grain size, temperature, and external size parameter or diameter with the failure mechanism. In the later part of the thesis, creep phenomenon in the nanocrystalline  $W$  has been explored. The conclusions of the thesis are summarized in the following sections.

### 5.1 Tensile Behavior of Single Crystal Nanowire

The computational experiments involving single crystal  $W$  nanowires revealed the importance of temperature, diameter, and loading direction on the mechanical properties of the nanowires. It is found that increasing temperature makes the nanowire act in more ductile manner. Moreover, at higher temperatures both stiffness and yield points of the nanowires decrease. This outcome is quite obvious. However, interesting results have been observed for variation in diameter and loading orientation. For diameters less than 5 nm, the fracture mechanism remains ductile. However, for nanowires with diameter of 5 nm, the failure mode suddenly shifts to brittle mode of failure with sudden increase in yield point. For nanowires greater than this size the failure mechanism remains brittle. For loading along  $\langle 111 \rangle$  direction, yield point reaches maximum. This occurs because

the  $\langle 111 \rangle$  surface is the energetically most stable surface. Hence, it takes higher load to rupture the nanowire. Additionally, deformation mechanism depends greatly on the loading orientation. In all the cases with applied loading along  $\langle 100 \rangle$  direction, primary deformation mechanism is twinning deformation. However, in case of applied loading along  $\langle 111 \rangle$  and  $\langle 112 \rangle$  directions, the primary deformation mechanism is slip or sudden failure. It infers that stacking of atoms in a material influences its failure mechanism profoundly.

## 5.2 Tensile Behavior of Polycrystalline Nanowire

It has been observed that under a critical grain size of 14.91 nm, plasticity is governed by inverse Hall-Petch relation. Within the framework of simulation, original Hall-Petch equation is modified for small grain size in polycrystalline  $W$  nanowire. From simulations it is also observed that root cause of inverse Hall-Petch effect is the dominance of grain boundary sliding over twinning deformation during fracture. Strength of nanowire follows an inverse relationship with diameter irrespective of temperature and grain size. Moreover, diameter of nanowire significantly alters the fracture mechanism. For small diameter nanowires failure is dominated by twinning in a single grain. Elevated temperature tends to reduce the strength of nanowires. However, there is no significant change in the failure mechanism at higher temperature.

## 5.3 Creep in Nanocrystalline Tungsten

In this work it is observed that creep phenomenon in nanocrystalline  $W$  can be lattice diffusion, grain boundary sliding or diffusion and dislocation-creep depending on the grain size, temperature and applied stress. Nanocrystalline  $W$  is more susceptible to creep deformation compared to the single crystal tungsten. There is no obvious creep phenomenon in single crystal  $W$  for a particular temperature and stress while nanocrystalline  $W$  may suffer significant creep for the same stress and temperature. This distinction corroborates to the previous studies using molecular dynamics simulation. As the grain size of nanocrystalline  $W$  is decreased the propensity of creep deformation increases. This occurs due to high volume of grain boundary in the sample which acts

as fast diffusion path and source and sink of dislocation. Applied stress is another key factor dictating the creep in  $W$  nanocrystal. By gradually increasing the applied stress one can achieve different creep mechanisms in nanocrystalline  $W$ . The primary creep mechanism is found to be lattice and grain boundary diffusion for low to moderate temperature and stress. Mean square displacement and diffusion co-efficients are analyzed to quantify the diffusion in nanocrystalline  $W$ . However, for fine grain size and high temperature and stress, the creep mechanism changes to dislocation creep. Grain size and stress exponents are used to construe the underlying physics of creep. The simulations show that for very high value of applied stress the power-law breaks down and can not sufficiently describe the creep phenomenon. Finally, atomic configurations are investigated which reveals lattice diffusion, grain boundary diffusion and dislocation creep is the order of dominant creep mechanism in nanocrystalline  $W$ . However, these process are not mutually exclusive.

# Bibliography

- [1] M. J. Buehler. *Atomistic modeling of materials failure*. Springer Science & Business Media, 2008.
- [2] R. P. Feynman. There's plenty of room at the bottom. *Engineering and science*, 23(5):22–36, 1960.
- [3] Z. Guo and L. Tan. *Fundamentals and applications of nanomaterials*. Artech House, 2009.
- [4] F. Sanchez and K. Sobolev. Nanotechnology in concrete—a review. *Construction and building materials*, 24(11):2060–2071, 2010.
- [5] D. L. Schodek, P. Ferreira, and M. F. Ashby. *Nanomaterials, nanotechnologies and design: an introduction for engineers and architects*. Butterworth-Heinemann, 2009.
- [6] M. S. Johal. *Understanding nanomaterials*. CRC Press, 2011.
- [7] L. Li. Molecular dynamics simulations of the deformation of nano-structured materials. 2007.
- [8] J. N. Tiwari, R. N. Tiwari, and K. S. Kim. Zero-dimensional, one-dimensional, two-dimensional and three-dimensional nanostructured materials for advanced electrochemical energy devices. *Progress in Materials Science*, 57(4):724–803, 2012.
- [9] L. Landström, J. Kokavecz, J. Lu, and P. Heszler. Characterization and modeling of tungsten nanoparticles generated by laser-assisted chemical vapor deposition. *Journal of applied physics*, 95(8):4408–4414, 2004.



- [10] S. S. Li. Classification of solids and crystal structure. In *Semiconductor Physical Electronics*, pages 1–25. Springer, 2006.
- [11] D. Hull and D. J. Bacon. *Introduction to dislocations*, volume 37. Elsevier, 2011.
- [12] T. Courtney, M. S. Sacks, J. Stankus, J. Guan, and W. R Wagner. Design and analysis of tissue engineering scaffolds that mimic soft tissue mechanical anisotropy. *Biomaterials*, 27(19):3631–3638, 2006.
- [13] S. Li, X. Ding, J. Deng, T. Lookman, J. Li, X. Ren, J. Sun, and A. Saxena. Superelasticity in bcc nanowires by a reversible twinning mechanism. *Physical Review B*, 82(20):205435, 2010.
- [14] E. O. Hall. The deformation and ageing of mild steel: Iii discussion of results. *Proceedings of the Physical Society. Section B*, 64(9):747, 1951.
- [15] N. J. Petch. The cleavage strength of polycrystals. *J. Iron Steel Inst.*, 174:25–28, 1953.
- [16] K. Lu and M. L. Sui. An explanation to the abnormal hall-petch relation in nanocrystalline materials. *Scripta metallurgica et materialia*, 28(12):1465–1470, 1993.
- [17] G.J. Fan, H. Choo, P. K. Liaw, and E. J. Lavernia. A model for the inverse hall–petch relation of nanocrystalline materials. *Materials Science and Engineering: A*, 409(1):243–248, 2005.
- [18] C. E. Carlton and P. J. Ferreira. What is behind the inverse hall–petch effect in nanocrystalline materials? *Acta Materialia*, 55(11):3749–3756, 2007.
- [19] Y. Tang, E. M. Bringa, and M. A. Meyers. Inverse hall–petch relationship in nanocrystalline tantalum. *Materials Science and Engineering: A*, 580:414–426, 2013.
- [20] S. S. Quek, Z. H. Chooi, Z. Wu, Y. W. Zhang, and D. J. Srolovitz. The inverse hall–petch relation in nanocrystalline metals: A discrete dislocation dynamics analysis. *Journal of the Mechanics and Physics of Solids*, 88:252–266, 2016.

- [21] H. W. Song, S. R. Guo, and Z. Q. Hu. A coherent polycrystal model for the inverse hall-petch relation in nanocrystalline materials. *Nanostructured Materials*, 11(2): 203–210, 1999.
- [22] W. D. Callister and D. G. Rethwisch. *Materials science and engineering*, volume 5. John Wiley & Sons NY, 2011.
- [23] A. K. Mukherjee, J. E. Bird, and J. E. Dorn. Experimental correlations for high-temperature creep. 1968.
- [24] H. W. Ch Postma, I. Kozinsky, A. Husain, and M.L. Roukes. Dynamic range of nanotube-and nanowire-based electromechanical systems. *Applied Physics Letters*, 86(22):223105, 2005.
- [25] Y. Zhang and H. Huang. Do twin boundaries always strengthen metal nanowires? *Nanoscale research letters*, 4(1):34, 2008.
- [26] G. Rubio-Bollinger, S. R. Bahn, N. Agrait, K. W. Jacobsen, and S. Vieira. Mechanical properties and formation mechanisms of a wire of single gold atoms. *Physical Review Letters*, 87(2):026101, 2001.
- [27] H. A. Wu. Molecular dynamics study on mechanics of metal nanowire. *Mechanics Research Communications*, 33(1):9–16, 2006.
- [28] H. Liu and J. Zhou. Plasticity in nanotwinned polycrystalline ni nanowires under uniaxial compression. *Materials Letters*, 163:179–182, 2016.
- [29] B. Wu, A. Heidelberg, and J. J. Boland. Mechanical properties of ultrahigh-strength gold nanowires. *Nature materials*, 4(7):525–529, 2005.
- [30] A. T. Jennings and J. R. Greer. Tensile deformation of electroplated copper nanopillars. *Philosophical Magazine*, 91(7-9):1108–1120, 2011.
- [31] C. Peng, Y. Zhong, Y. Lu, S. Narayanan, T. Zhu, and J. Lou. Strain rate dependent mechanical properties in single crystal nickel nanowires. *Applied Physics Letters*, 102(8):083102, 2013.
- [32] D. Chen and T. Chen. Mechanical properties of au nanowires under uniaxial tension with high strain-rate by molecular dynamics. *Nanotechnology*, 16(12):2972, 2005.

- [33] J. Diao, K. Gall, and M. L. Dunn. Yield strength asymmetry in metal nanowires. *Nano Letters*, 4(10):1863–1867, 2004.
- [34] H. S. Park and J. A. Zimmerman. Stable nanobridge formation in  $\text{Au}$  gold nanowires under tensile deformation. *Scripta Materialia*, 54(6):1127–1132, 2006.
- [35] S. K. Deb Nath and S. Kim. On the elastic, elastic-plastic properties of Au nanowires in the range of diameter 1-200 nm. *Journal of Applied Physics*, 112(12):123522, 2012.
- [36] S.J.A. Koh, H.P. Lee, C. Lu, and Q.H. Cheng. Molecular dynamics simulation of a solid platinum nanowire under uniaxial tensile strain: Temperature and strain-rate effects. *Physical Review B*, 72(8):085414, 2005.
- [37] Z.X. Wu, Y.W. Zhang, M.H. Jhon, J.R. Greer, and D.J. Srolovitz. Nanostructure and surface effects on yield in Cu nanowires. *Acta Materialia*, 61(6):1831–1842, 2013.
- [38] F. Wang, W. Sun, Y. Gao, Y. Liu, J. Zhao, and C. Sun. Investigation on the most probable breaking behaviors of copper nanowires with the dependence of temperature. *Computational Materials Science*, 67:182–187, 2013.
- [39] S.K. Deb Nath. Elastic, elastic-plastic properties of Ag, Cu and Ni nanowires by the bending test using molecular dynamics simulations. *Computational Materials Science*, 87:138–144, 2014.
- [40] P. S. Branício and J. Rino. Large deformation and amorphization of Ni nanowires under uniaxial strain: a molecular dynamics study. *Physical Review B*, 62(24):16950, 2000.
- [41] A. Setoodeh, H. Attariani, and M. Khosrownejad. Nickel nanowires under uniaxial loads: A molecular dynamics simulation study. *Computational Materials Science*, 44(2):378–384, 2008.
- [42] Y. Wen, Z. Zhu, and R. Zhu. Molecular dynamics study of the mechanical behavior of nickel nanowire: Strain rate effects. *Computational Materials Science*, 41(4):553–560, 2008.

- [43] G. Sainath and B.K. Choudhary. Orientation dependent deformation behaviour of bcc iron nanowires. *Computational Materials Science*, 111:406–415, 2016.
- [44] P. Wang, W. Chou, A. Nie, Y. Huang, H. Yao, and H. Wang. Molecular dynamics simulation on deformation mechanisms in body-centered-cubic molybdenum nanowires. *Journal of Applied Physics*, 110(9):093521, 2011.
- [45] A. Cao. Shape memory effects and pseudoelasticity in bcc metallic nanowires. *Journal of Applied Physics*, 108(11):113531, 2010.
- [46] C. Fenster, A. J. Smith, A. Abts, S. Milenkovic, and A. W. Hassel. Single tungsten nanowires as ph sensitive electrodes. *Electrochemistry Communications*, 10(8):1125–1128, 2008.
- [47] J. Chang, Y. Yang, and L. Wang. Tungsten nanowire based hyperbolic metamaterial emitters for near-field thermophotovoltaic applications. *International Journal of Heat and Mass Transfer*, 87:237–247, 2015.
- [48] Y. Lee, C. Choi, Y. Jang, E. Kim, B. Ju, N. Min, and J. Ahn. Tungsten nanowires and their field electron emission properties. *Applied Physics Letters*, 81(4):745–747, 2002.
- [49] J. Wang, Z. Zeng, C. R. Weinberger, Z. Zhang, T. Zhu, and S. X. Mao. In situ atomic-scale observation of twinning-dominated deformation in nanoscale body-centred cubic tungsten. *Nature materials*, 14(6):594–600, 2015.
- [50] B. Ma, Q. Rao, and Y. He. Molecular dynamics simulation of temperature effect on tensile mechanical properties of single crystal tungsten nanowire. *Computational Materials Science*, 117:40–44, 2016.
- [51] V. Cimalla, C.-C. Röhlig, J. Pezoldt, M. Niebelschütz, O. Ambacher, K. Brückner, M. Hein, J. Weber, S. Milenkovic, A. J. Smith, et al. Nanomechanics of single crystalline tungsten nanowires. *Journal of Nanomaterials*, 2008:44, 2008.
- [52] N. Hansen. Hall–petch relation and boundary strengthening. *Scripta Materialia*, 51(8):801–806, 2004.
- [53] C. Deng and F. Sansoz. Enabling ultrahigh plastic flow and work hardening in twinned gold nanowires. *Nano letters*, 9(4):1517–1522, 2009.

- [54] X. Li, W. Hu, S. Xiao, and W.-Q. Huang. Molecular dynamics simulation of polycrystalline molybdenum nanowires under uniaxial tensile strain: size effects. *Physica E: Low-dimensional Systems and Nanostructures*, 40(10):3030–3036, 2008.
- [55] A. Cao, Y. Wei, and E. Ma. Grain boundary effects on plastic deformation and fracture mechanisms in cu nanowires: Molecular dynamics simulations. *Physical Review B*, 77(19):195429, 2008.
- [56] Y. Zhu, Z. Li, and M. Huang. Coupled effect of sample size and grain size in polycrystalline al nanowires. *Scripta Materialia*, 68(9):663–666, 2013.
- [57] R.L. Coble. A model for boundary diffusion controlled creep in polycrystalline materials. *Journal of applied physics*, 34(6):1679–1682, 1963.
- [58] C. Herring. Diffusional viscosity of a polycrystalline solid. *Journal of applied physics*, 21(5):437–445, 1950.
- [59] Y.-J. Wang, A. Ishii, and S. Ogata. Grain size dependence of creep in nanocrystalline copper by molecular dynamics. *Materials Transactions*, 53(1):156–160, 2012.
- [60] X.-S. Yang, Y.-J. Wang, H.-R. Zhai, G.-Y. Wang, Y.-J. Su, L.H. Dai, S. Ogata, and T.-Y. Zhang. Time-, stress-, and temperature-dependent deformation in nanostructured copper: Creep tests and simulations. *Journal of the Mechanics and Physics of Solids*, 94:191–206, 2016.
- [61] K. Nie, W.-P. Wu, X.-L. Zhang, and S.-M. Yang. Molecular dynamics study on the grain size, temperature, and stress dependence of creep behavior in nanocrystalline nickel. *Journal of Materials Science*, 52(4):2180–2191, 2017.
- [62] V. Yamakov, D. Wolf, S. R. Phillpot, and H. Gleiter. Grain-boundary diffusion creep in nanocrystalline palladium by molecular-dynamics simulation. *Acta Materialia*, 50(1):61–73, 2002.
- [63] A. J. Haslam, V. Yamakov, D. Moldovan, D. Wolf, S.R. Phillpot, and H. Gleiter. Effects of grain growth on grain-boundary diffusion creep by molecular-dynamics simulation. *Acta Materialia*, 52(7):1971–1987, 2004.

- [64] P. Keblinski, D. Wolf, and H. Gleiter. Molecular-dynamics simulation of grain-boundary diffusion creep. *Interface Science*, 6(3):205–212, 1998.
- [65] W.M. Yin, S.H. Whang, R. Mirshams, and C.H. Xiao. Creep behavior of nanocrystalline nickel at 290 and 373 k. *Materials Science and Engineering: A*, 301(1):18–22, 2001.
- [66] N. Karanjgaokar and I. Chasiotis. Creep behavior of nanocrystalline au films as a function of temperature. *Journal of materials science*, 51(8):3701–3714, 2016.
- [67] S. Jiao and Y. Kulkarni. Molecular dynamics study of creep mechanisms in nanotwinned metals. *Computational Materials Science*, 110:254–260, 2015.
- [68] Y. Wang, A. Ishii, and S. Ogata. Transition of creep mechanism in nanocrystalline metals. *Physical Review B*, 84(22):224102, 2011.
- [69] F. Khabaz, K. S. Khare, and R. Khare. Temperature dependence of creep compliance of highly cross-linked epoxy: A molecular simulation study. In *AIP Conference Proceedings*, volume 1599, pages 262–265. AIP, 2014.
- [70] M.A. Bhatia, S.N. Mathaudhu, and K.N. Solanki. Atomic-scale investigation of creep behavior in nanocrystalline mg and mg–y alloys. *Acta Materialia*, 99:382–391, 2015.
- [71] J. Li, J.Y. Zhang, P. Zhang, K. Wu, G. Liu, and J. Sun. Grain size effects on microstructural stability and creep behaviour of nanotwinned ni free-standing foils at room temperature. *Philosophical Magazine*, 96(29):3016–3040, 2016.
- [72] S. Pal, Md. Meraj, and C. Deng. Effect of zr addition on creep properties of ultra-fine grained nanocrystalline ni studied by molecular dynamics simulations. *Computational Materials Science*, 126:382–392, 2017.
- [73] G.W. King. The stress-dependence of high temperature creep of tungsten and a tungsten-2 wt pct tho 2 alloy. *Metallurgical and Materials Transactions B*, 3(4):941–945, 1972.
- [74] S.L. Robinson and O.D. Sherby. Mechanical behavior of polycrystalline tungsten at elevated temperature. *Acta Metallurgica*, 17(2):109–125, 1969.

- [75] C. R. Weinberger and G. J. Tucker. *Multiscale Materials Modeling for Nanomechanics*, volume 245. Springer, 2016.
- [76] J.M. Haile, I. Johnston, A. J. Mallinckrodt, S. McKay, et al. Molecular dynamics simulation: elementary methods. *Computers in Physics*, 7(6):625–625, 1993.
- [77] A. C.T. Van Duin, S. Dasgupta, F. Lorant, and W. A. Goddard. Reaxff: a reactive force field for hydrocarbons. *The Journal of Physical Chemistry A*, 105(41):9396–9409, 2001.
- [78] C.S. Murthy, S.F. O’Shea, and I.R. McDonald. Electrostatic interactions in molecular crystals: lattice dynamics of solid nitrogen and carbon dioxide. *Molecular Physics*, 50(3):531–541, 1983.
- [79] H. Noorian, D. Toghraie, and A.R. Azimian. Molecular dynamics simulation of poiseuille flow in a rough nano channel with checker surface roughnesses geometry. *Heat and mass transfer*, 50(1):105–113, 2014.
- [80] J. Nocedal and S. J. Wright. Conjugate gradient methods. *Numerical optimization*, pages 101–134, 2006.
- [81] J. Schiøtz, T. Vegge, F.D. Di Tolla, and K. W. Jacobsen. Atomic-scale simulations of the mechanical deformation of nanocrystalline metals. *Physical Review B*, 60(17):11971, 1999.
- [82] P. Hirel. AtomsK: A tool for manipulating and converting atomic data files. *Computer Physics Communications*, 197:212–219, 2015.
- [83] N. Chandra, S. Namilaee, and C. Shet. Local elastic properties of carbon nanotubes in the presence of stone-wales defects. *Physical Review B*, 69(9):094101, 2004.
- [84] M. Zhou. A new look at the atomic level virial stress: on continuum-molecular system equivalence. In *Proceedings of the Royal Society of London A: Mathematical, Physical and Engineering Sciences*, volume 459, pages 2347–2392. The Royal Society, 2003.
- [85] S. Pal and Md. Meraj. Structural evaluation and deformation features of interface of joint between nano-crystalline Fe–Ni–Cr alloy and nano-crystalline Ni during creep process. *Materials & Design*, 108:168–182, 2016.

- [86] X.W. Zhou, R.A. Johnson, and H.N.G. Wadley. Misfit-energy-increasing dislocations in vapor-deposited co/nife multilayers. *Physical Review B*, 69(14):144113, 2004.
- [87] H. H. Landolt, R. Börnstein, K.-H. Hellwege, J. Bystricky, and H. Schopper. *Numerical data and functional relationships in science and technology: new series. Nuclear and particle physics. Elastic and charge exchange scattering of elementary particles. Nucleon nucleon and kaon nucleon scattering*, volume 9. Springer., 1980.
- [88] A. Moitra, S. Kim, J. Houze, B. Jelinek, S.-G. Kim, S. Park, R. M. German, and M. F. Horstemeyer. Melting tungsten nanoparticles: a molecular dynamics study. *Journal of Physics D: Applied Physics*, 41(18):185406, 2008.
- [89] S. Plimpton. Fast parallel algorithms for short-range molecular dynamics. *Journal of computational physics*, 117(1):1–19, 1995.
- [90] A. Stukowski. Visualization and analysis of atomistic simulation data with ovito—the open visualization tool. *Modelling and Simulation in Materials Science and Engineering*, 18(1):015012, 2009.
- [91] C. Begau, J. Hua, and A. Hartmaier. A novel approach to study dislocation density tensors and lattice rotation patterns in atomistic simulations. *Journal of the Mechanics and Physics of Solids*, 60(4):711–722, 2012.
- [92] A. Stukowski and K. Albe. Extracting dislocations and non-dislocation crystal defects from atomistic simulation data. *Modelling and Simulation in Materials Science and Engineering*, 18(8):085001, 2010.
- [93] M.A. Bin, Q. Rao, and Y. He. Effect of crystal orientation on tensile mechanical properties of single-crystal tungsten nanowire. *Transactions of Nonferrous Metals Society of China*, 24(9):2904–2910, 2014.